Fluctuating oxygenation and dynamic iron cycling in the late Paleoproterozoic ocean.

Article:

Yang, X., Mao, J., Li, R. et al. (7 more authors) (Cover date: 15 January 2024) Fluctuating oxygenation and dynamic iron cycling in the late Paleoproterozoic ocean. Earth and Planetary Science Letters, 626. 118554. ISSN 0012-821X

https://doi.org/10.1016/j.epsl.2023.118554

Fluctuating oxygenation and dynamic iron cycling in the late Paleoproterozoic ocean

Xiuqing Yang [a, b, *], Jingwen Mao [a, c], Rongxi Li [a, c], Fang Huang [d], Chong He [b], Chao Zhao [a], Wei Wei [d], Guowei Yang [a], Yijun Xiong [b], Simon W. Poulton [b]

[a] MOE Key Laboratory of Western China's Mineral Resources and Geological Engineering, School of Earth Science and Resources, Chang'an University, Xi'an 710054, China
[b] School of Earth and Environment, University of Leeds, Leeds LS2 9JT, UK
[c] MNR Key Laboratory for Exploration Theory & Technology of Critical Mineral Resources, China University of Geosciences (Beijing), Beijing 100083, China
[d] CAS Key Laboratory of Crust-Mantle Materials and Environments, School of Earth and Space Sciences, University of Science and Technology of China, Hefei 230026, China

* *E-mail address*: xiuqing2008@126.com (X. Yang).

Abstract

The mid-Proterozoic (1.8–0.8 billion years ago, Ga) is generally considered to have been an interval of relative stasis in terms of environmental and biological evolution. Indeed, in terms of ocean redox chemistry, deeper ocean waters are considered to have dominantly remained anoxic and ferruginous throughout this interval. Despite the persistence of ferruginous conditions, the mid-Proterozoic has long been considered notable for a general absence of iron formations (IFs), in stark contrast to the major intervals of IF deposition that occurred in the ferruginous oceans of the earlier Precambrian. In recent years, however, sporadic IFs have been found in the mid-Proterozoic, but controls on the genesis of these IFs, as well as implications for the evolution of ocean chemistry, remain poorly understood. Here, we present major and trace element data, iron speciation systematics, and organic carbon and iron isotope data for the ~1.64 Ga Chuanlinggou Formation, which hosts a sudden reappearance of substantial IF deposition on the North China Craton. The Chuanlinggou IF has low Y/Ho ratios (24–26), slightly positive Eu anomalies ($Eu/Eu^* = 1.14–1.47$), no Ce anomalies, slightly positive $\delta^{56}Fe$ values (0.05 to 0.35‰), and high $\delta^{13}C_{org}$ values (-29‰) relative to deeper water facies (down to -33.4‰). These observations provide support for a redox-stratified ocean with oxic surface waters overlying ferruginous deeper waters, and further suggest that IF deposition occurred in a stratified ocean with a shallow redoxcline during an interval of elevated Fe concentrations. Specifically, we suggest that the development of relatively intense ferruginous conditions was likely a consequence of hydrothermal activity during the breakup of the Columbia supercontinent. Microaerophilic iron-oxidizing bacteria and/or anoxygenic photosynthesizers likely played a key role in the generation of the Chuanlinggou IF. Importantly, however, data for shales that overly the Chuanlinggou IF suggest episodic intervals of deeper water oxygenation. Thus, similar to recent studies of the later Mesoproterozoic ocean, our data indicate that ocean chemistry during the latest Paleoproterozoic may have been more dynamic than previously considered, with fluctuating oxygen and iron levels likely exerting a limiting constraint on both the evolution of eukaryotes and the deposition of IFs across the immense interval of time encapsulated by the mid-Proterozoic.

Keywords: iron formations; Proterozoic; ocean oxygenation; iron isotopes; Chuanlinggou iron formation

1. Introduction

It is generally accepted that the Archean atmosphere and oceans were largely anoxic, with the exception of 'oxygen oases', representing regions of relatively shallow water oxygenation that became progressively more widespread during the Neoarchean (e.g., Ostrander et al., 2019; Ossa Ossa et al., 2019). However, shallow water oxygenation became particularly expansive following Earth's first major rise in atmospheric oxygen, which occurred during the Great Oxidation Event (GOE) around 2.4 to 2.1 billion years (Ga) ago (e.g., Holland, 1984; Poulton et al., 2021). During the GOE, atmospheric O_2 rose in a fluctuating manner (Gumsley et al., 2018; Poulton et al., 2021) to levels above 10^{-6} of the present atmospheric level (PAL; Zahnle et al., 2006). Subsequently, the Paleoproterozoic ocean is widely considered to have been redox-stratified (e.g., Planavsky et al., 2011; Poulton and Canfield, 2011), with a possible decrease in atmospheric O_2 levels after peak concentrations towards the end of the GOE (e.g., Ossa Ossa et al., 2022). A second interval of highly fluctuating atmospheric oxygen levels (between ~10-50% PAL) occurred during the Neoproterozoic Oxygenation Event (NOE) between ~900 and 540 million years (Ma) ago (Krause et al., 2022), before atmospheric oxygen levels rose to near modern levels during the Paleozoic Oxygenation Event (POE; e.g., Krause et al., 2018).

The mid-Proterozoic (1.8–0.8 Ga) encapsulates a major proportion of time between the GOE and the NOE, and is considered to have been a prolonged interval of relative stasis in terms of both Earth surface oxygenation and the evolution of eukaryotic organisms (e.g., Zhang et al., 2016, 2018). However, oxygen levels in the atmosphere and surface ocean, as well as the chemical composition of the deeper ocean, remain topics of considerable debate. A general view of a mid-Proterozoic ocean characterized by oxygenated surface waters, with anoxic and sulfidic waters in mid-depths along productive continental margins, and anoxic ferruginous deeper waters has emerged (e.g., Poulton and Canfield, 2011; Planavsky et al., 2011). However, recent evidence has documented more dynamic redox conditions, with pulses of water column oxygenation at 1.57–1.56 Ga (e.g., Zhang et al., 2018; Luo et al., 2021), ~1.4 Ga (e.g., Zhang et al., 2016) and ~1.33 Ga (Canfield et al., 2018a), and significant spatial heterogeneity driven by global climatic variability (e.g., Song et al., 2023).

The deposition of iron formations (IFs) represents a major line of evidence for ferruginous oceanic conditions through the Archean and earlier Paleoproterozoic (up until ~1.88 Ga) (e.g., Bekker et al., 2010). Deposition of IFs requires the oceans to have been sufficiently reducing to allow transport and storage of large quantities of aqueous Fe(II). During IF deposition Fe(II) was oxidized, commonly in the photic zone by local cyanobacterial O_2 production or via direct metabolic Fe(II) oxidation (e.g., by chemolithoautotrophic iron-oxidizing bacteria (FeOB) or anoxygenic photosynthesizers; Bekker et al., 2010; Konhauser et al., 2017). However, despite evidence for persistent anoxia and ferruginous deeper waters, substantial deposition of IFs is commonly considered not to have occurred during the mid-Proterozoic (e.g., Bekker et al., 2010). Recent reports have, however, documented the occurrence of major IFs at ~1.64 Ga (Lin et al., 2019 and references therein) and ~1.4 Ga (Canfield et al., 2018b), thereby questioning this paradigm. Nevertheless, IF deposition during the mid-Proterozoic appears to have been rare relative to earlier in Earth's history, and controls on the genesis of mid-Proterozoic IFs, as well as detailed implications for the evolution of ocean redox conditions, have received little attention.

Here, we focus on the ~1.64 Ga Chuanlinggou Formation (CF) in the Yanliao Basin, North China Craton (NCC) (Fig. 1a), where ~4700 million tons of IF-type hematite ore occurs (Lin et al., 2019), representing the first large IF deposit after their apparent demise at ~1.88 Ga (Bekker et al., 2010). We utilize major and trace element data, Fe speciation systematics, and Fe and organic C isotope data to assess the evolution of water column redox conditions and controls on IF genesis. In doing so, our data provide a direct assessment of marine redox conditions and iron cycling towards the end of the Paleoproterozoic era (~1.64 Ga), with broader scale implications for the IF record and eukaryotic evolution across the mid-Proterozoic.

2. Geological setting

The Yanliao Basin formed via a continental rift that developed on the northern margin of the NCC beginning at ~1.7 Ga, possibly linked to the early break-up of the Columbia Supercontinent (Fig. 1b; Kusky and Li, 2003). Sedimentary rocks in the Yanliao Basin contain the 1.8–1.6 Ga Changcheng Group, the 1.6–1.4 Ga Jixian Group, the 1.4–1.0 Ga Huailai group, and 1.0–0.8 Ga Qingbaikou Group (Fig. 1c; Zhu et al., 2016; Lin et al., 2019).

The 1.8–1.6 Ga Changcheng Group was deposited on Archean-early Paleoproterozoic crystalline basement, and in stratigraphic order consists of the Changzhougou, Chuanlinggou, Tuanshanzi and Dahongyu formations. During the latest Paleoproterozoic, the Yanliao Basin was likely connected to the open ocean in the north, and the transgression of seawater into the basin was from the northwest or northeast (Lin et al., 2019). The Changzhougou Formation is dominated by fluvial coarse sandstones and conglomerates in its lower portion, and by littoral-intertidal siltstones and sandstones in its upper portion, representing the initial development of the Yanliao Basin. IFs, dolostones, black shales and interbedded sandstones of the CF record a transition from a shallow marine environment to a subtidal low-energy environment (e.g., Li et al., 2015; Lin et al., 2019) (Figs. 2a and b). Volcanic rocks in the Tuanshanzi and Dahongyu formations mark the peak development of the basin.

The 1.6–1.4 Ga Jixian Group, including the Gaoyuzhuang, Yangzhuang, Wumishan, Hongshuizhuang and Tieling Formations, is dominated by carbonate rocks, including laminated and stromatolitic dolostone, limestone, muddy dolostone and chert bands. The younger ~1.4 Ga Xiamaling Formation consists of black shale, muddy dolostone, mudstone and IFs (Zhang et al., 2016; Canfield et al., 2018b). The 1.0–0.8 Ga Qingbaikou Group, which mainly consists of sandstone and shale, marks the return of dominantly siliciclastic deposition prior to regional uplift of the Yanliao Basin (Fig. 1c; Luo et al., 2014; Li et al., 2015; Zhang et al., 2018).

The CF documents a basin-scale water depth gradient running from north to south, with deeper water facies deposited in the south along a narrow belt bounded by two sets of NE- to SW-trending rift faults (Beijing–Lingyuan and Luanxian–Jianchang; Li et al., 2015). The CF is widely distributed on the NCC and can be divided into three depositional areas. The eastern area, including Jixian, Zunhua, Xinglong and Kuancheng, is characterized by the development of thick black shales. The middle area is located in the northern part of Miyun–Huairou and comprises thick stromatolitic dolostones and lagoonal facies deposition. The western area is located in the Xuanhua–Zhangjiakou area, where the CF is significantly thinner and characterized by the development of IFs. Regionally the IFs extend for ~154 km in a NS direction and ~130 km in a WE direction, and cover an area of ~3900 km^2. The western area, with an estimated total iron ore resource of ~4700 Mt, is characterized by a thin depositional thickness (<50 m) and multiple layers of IF in its lower part (Fig. 2c). The CF is interpreted as a passive-margin sequence, suggesting a strong connection to the open ocean (Lin et al., 2019), and the depositional age of the CF can be constrained to ~1.64 Ga (see Supplementary Information Appendix A; Fig. 1c).

3. Materials and methods

3.1 Materials

Chuanlinggou Formation drill core samples were collected from the western area (Xuanhua-Chicheng-Longguan; hereon abbreviated to Xuan-Long), Hebei province. Samples comprise sandstone (n = 1) (Fig. 2d), IF (n = 12) (Fig. 2e), black shale (including two siderite-rich shales) (n = 87) (Fig. 2f), and dolostone (n = 32) (Fig. 2g), deposited under marine conditions ranging from a shallow subtidal/intertidal zone to a deeper subtidal setting (Fig. 2h; Supplementary Information Appendix A). Prior to analysis, samples were fragmented using a jaw crusher, followed by crushing to a fine powder in a Tema mill with a tungsten carbide barrel.

3.2 Carbon concentration analyses

Total organic carbon (TOC) and total carbon (TC) contents were obtained for all samples using a LECO C/S Analyzer in the Cohen Geochemistry Laboratory, University of Leeds. For TOC content, sample powders were first treated with 10% HCl to remove carbonate phases. Replicate analyses of certified standards (Soil 502–309, Soil 502–062, Calcium carbonate 501–034 and Coal 502–671) gave RSDs of < 2% for TC and < 2% for TOC, with close to 100% recovery in all cases. Total inorganic carbon (TIC) contents were calculated as TIC = TC – TOC, and replicates of TIC analyses gave a RSD of < 2%.

3.3 Organic carbon isotope analyses

Organic carbon isotope ($\delta^{13}C_{org}$) compositions were measured in the Analytical Laboratory of the Beijing Research Institute of Uranium Geology, Beijing, China. Powdered samples were first oven dried at 40°C and then dissolved with 0.5 N HCl to remove carbonate minerals, with residuals combusted at 900°C for 1 h to collect the CO_2 derived from organic matter. The resulting CO_2 was then dehydrated and purified before analysis via a Finnigan MAT-253 isotope mass spectrometer. Analyses of standard IAEA-600 (Caffeine, $\delta^{13}C_{org}$ = -27.771‰) gave an analytical precision of better than 0.1‰. Standards were measured every six samples to monitor and correct for potential drift. $\delta^{13}C_{org}$ values are reported in per mil (‰) notation relative to the Vienna Pee Dee Belemnite (V-PDB) standard.

3.4 Major and trace element analyses

Total element concentrations (Fe, Mn and Al) were determined on samples via an

HF-$HClO_4$-HNO_3 extraction, with HBO_3 used to ensure full solubilisation of Al, followed by analysis using a ThermoFisher iCAP 7400 radial inductively coupled plasma optical emission spectrometer (ICP-OES). Trace elements (Mo, U and V) were analysed on the same solutions using a ThermoFisher iCAP Qc inductively coupled plasma mass spectrometer (ICP-MS) in the Cohen Geochemistry Laboratory, University of Leeds. Accuracy was monitored relative to reference material USGS Eocene Green River Shale (SGR-1), with all elements being within 93 ± 6% of certified values. Repeat measurements of samples yielded RSDs for all elements of better than 3%.

Rare earth element (REEs), Y and Ba concentrations were obtained by an Agilent 7700x ICP-MS at the ALS Chemex, Guangzhou, China. Briefly, 50 mg of sample powder was melted in $LiBO_2$/$Li_2B_4O_7$ solvent and heated at 1025°C. The sample was then dissolved using a $HClO_4$, HNO_3 and HF mixture, then evaporated to near dryness and dissolved in dilute HCl to 100 mL. Certified standards MRGeo08 (granite), GBM908-10 (oxide copper gold ore), OREAS 25 (mature soil) and OREAS 25 (a blend of mineralized ferruginous soil and barren mature soil) were used as standards during the analyses. Analytical uncertainties are ± 5% for REEs, and ± 5–10% for other trace elements.

3.5 Iron isotope analyses

Bulk-rock Fe isotope compositions were analyzed at the Key Laboratory of Crust-Mantle Materials and Environments, University of Science and Technology of China, Hefei, China. Fe was purified using anion resin (Bio-Rad AG1-X8) conditioned with 8 N HCl, and matrix elements were removed by washing with 8 N HCl. Fe was eluted using 0.5 N HCl and H_2O followed by 8 N HNO_3 and H_2O. A pure Fe solution with high yield was obtained by two passes through the column for all samples. Standard bracketing methods were followed (Huang et al., 2011), and analyses were performed on a Neptune Plus MC-ICP-MS. Iron solutions were diluted to 1.5 ppm for analysis and bracketed with IRMM-14 at the same concentration. ^{54}Fe, ^{56}Fe and ^{57}Fe (along with ^{53}Cr for correcting any ^{54}Cr interference) were measured in static mode on L3, H4 and H6 Faraday cups, respectively. Contributions from isobaric interferences (^{40}Ar^{14}N on ^{54}Fe and ^{40}Ar^{16}O on ^{56}Fe) were eliminated by measuring in pseudo-high resolution mode with M/ΔM of ~8000. Iron isotope results are reported as ‰ in the standard delta notation:

$$\delta^{56}\text{Fe}\ (‰) = 1000 \times [(^{56}\text{Fe}/^{54}\text{Fe})_{\text{sample}} / (^{56}\text{Fe}/^{54}\text{Fe})_{\text{IRMM-14}} - 1]$$

The international geological reference standards BHVO-2 = 0.11 ± 0.01‰, BIR-1 = 0.05 ± 0.01‰, RGM-1 = 0.21 ± 0.05‰, were analyzed repeatedly to monitor the external reproducibility, were within the error of certified values (Huang et al., 2011 and references therein).

3.6 Iron speciation analyses

Iron speciation analyses were conducted following the sequential extraction procedure of Poulton and Canfield (2005) in the Cohen Geochemistry Laboratory, University of Leeds. Extractions were performed according to the calibrated procedure, whereby carbonate-associated Fe (e.g., siderite, ankerite; Fe_{carb}) was targeted with Na-acetate at pH 4.5 and 50°C for 48 h, ferric (oxyhydr)oxides (e.g., goethite, hematite; Fe_{ox}) were targeted using Na-dithionite at pH 4.8 for 2 h, and magnetite (Fe_{mag}) was targeted by an ammonium oxalate extraction for 6 h. Sulfide-bound Fe was determined via the two-step chromous chloride distillation procedure of Canfield et al. (1986). Acid volatile sulfide (Fe_{AVS}; below detection in all cases) was extracted with boiling 6 N HCl, and pyrite (Fe_{py}) was extracted with boiling chromous chloride. The liberated sulfide was trapped as Ag_2S, and Fe_{py} was determined gravimetrically. Accuracy was ensured by repeat analyses of international sediment standard WHIT, with RSDs of <5% for all stages.

4. Interpretational framework

4.1 Redox reconstruction

We use four independent approaches to assess water column redox conditions: REE+Y, Fe speciation, Fe_T/Al (where Fe_T represents total Fe) ratios and redox-sensitive trace element (RSE) systematics. The capture and preservation of aqueous REE+Y patterns in IFs provide a window into ancient ocean chemistry and redox state. In general, modern oxygenated seawater is characterized by a strong negative Ce anomaly when normalized to Post-Archean Average Shale (PAAS, Supplementary Information Appendix A; Byrne and Sholkovitz, 1996). This is because the oxidation of Ce(III) greatly reduces Ce solubility, resulting in preferential removal of Ce by Fe- and Mn-(oxyhydr)oxides, organic matter and clay particles. By contrast, dysoxic and anoxic waters lack true negative Ce anomalies (e.g., Planavsky et al., 2010). Yttrium and Ho act as a twin pair due to their similar charge and radius. Modern seawater is characterized by super-chondritic Y/Ho ratios of 44 to 74, significantly greater than both upper crustal rocks and chondritic Y/Ho ratios of 26–28 with no apparent fractionation of Y from Ho (Bau et al., 1996), which result from faster scavenging of Ho over Y by Fe- and Mn-(oxyhydr)oxides. When Fe- and Mn-(oxyhydr)oxide particles settle into dysoxic/anoxic deeper waters in a redox stratified ocean, a decrease in dissolved seawater Y/Ho ratios develops due to reductive dissolution (Bau et al., 1996; Planavsky et al., 2010).

Iron speciation data potentially allow oxic water column conditions to be distinguished from ferruginous (anoxic, Fe(II)-containing) and euxinic conditions (Poulton and Canfield, 2011; Poulton, 2021), whereby the biogeochemically highly reactive Fe pool (Fe_{HR}), including Fe_{carb}, Fe_{ox}, Fe_{mag} and Fe_{py}, is quantified relative to Fe_T. Iron speciation has been extensively calibrated in modern and ancient settings, and ancient oxic marine sediments commonly have $Fe_{HR}/Fe_T < 0.22$, whereas water column enrichments under anoxic conditions typically result in $Fe_{HR}/Fe_T > 0.38$ (Poulton and Canfield, 2011). Ratios between 0.22–0.38 are considered equivocal, and may represent either oxic or anoxic depositional conditions. For anoxic samples, ferruginous conditions are distinguished from euxinic conditions by quantifying the extent of pyritization of the highly reactive iron pool (Fe_{py}/Fe_{HR}). $Fe_{py}/Fe_{HR} > 0.8$ is characteristic of euxinic deposition, whereas $Fe_{py}/Fe_{HR} < 0.6$ indicates deposition under ferruginous conditions. Ratios between 0.6–0.8 are considered equivocal, and may represent either euxinic or ferruginous conditions (Poulton and Canfield, 2011; Poulton, 2021). Fe_T/Al ratios can also distinguish anoxic and oxic depositional environments, particularly in IF samples where enrichments in Fe_T/Al can be extreme, resulting in ratios that are highly elevated relative to the wide range of regional compositions that can occur due to the geochemical composition of the source material. Fe_T/Al ratios $> 0.55 \pm 0.11$ are commonly taken to indicate anoxic conditions (Clarkson et al., 2014).

We utilize the redox-dependent behaviour of Mo, U and V to provide further independent insight into redox conditions (e.g., Tribovillard et al., 2006). In oxygenated modern oceans, the conservative elements Mo and U mainly occur as soluble molybdate (MoO_4^{2-}) and uranyl carbonate complexes ($UO_2(CO_3)_3^{4-}$). High sediment Mo accumulation tends to occur through the formation of particle-reactive thiomolybdates when water-column concentrations of sulfide are high (e.g., Helz et al., 1996). By contrast, U may be fixed in the sediment under anoxic porewater conditions, without the requirement for free H_2S (e.g., Anderson et al., 1989). Such conditions also explain enrichments in vanadium, as the vanadate ion [$VO_2(OH)_3^{2-}$, V(V)] is reduced to immobile V(IV) and V(III) phases under reducing conditions (e.g., Emerson and Huested, 1991).

4.2 Fe cycling

Ferrous iron oxidation in reducing environments can be driven by local cyanobacterial O_2 production or by direct metabolic Fe(II) oxidation (e.g., by microaerophilic FeOB and anoxygenic photosynthesizers; Bekker et al., 2010; Konhauser et al., 2017). UV photo-oxidation has also been considered as a possible mechanism, but the efficiency of UV-dependent oxidation in complex seawater solutions has been questioned in recent experimental studies (Konhauser et al., 2017). Submarine hydrothermal-sourced Fe has a characteristic δ^{56}Fe value of -0.5 to 0.0‰, while seawater has a relatively homogeneous Fe isotope composition of close to 0‰ (Johnson et al., 2008). Biotic and abiotic partial oxidation of Fe(II) to Fe(III) in solution can cause large Fe isotope fractionations, typically in the region of 1.5 to >2.5‰ (Johnson et al., 2008; Planavsky et al., 2012). By contrast, complete oxidation and precipitation produces Fe-(oxyhydr)oxide δ^{56}Fe values equal to those of the initial Fe(II) (Johnson et al., 2008).

Whole rock δ^{56}Fe compositions reflect the net Fe isotopic composition of a mixture of different iron-bearing minerals, whose contents and isotopic compositions vary between samples. In this study, we use a simple mixing model to calculate δ^{56}Fe values of Fe_{HR}: $\delta^{56}Fe = (Fe_{HR} \times \delta^{56}Fe_{HR} + Fe_U \times \delta^{56}Fe_U)/(Fe_{HR} + Fe_U)$, where δ^{56}Fe is the measured whole rock value, $\delta^{56}Fe_{HR}$ is the isotopic composition of highly reactive iron, and $\delta^{56}Fe_U$ is the isotopic composition of unreactive iron, which we assume to have crustal values (i.e., 0.1‰; Planavsky et al., 2012).

5. Results

All data are listed in Supplementary Information Appendix B. In the lower CF, the 4 black shale samples have varying TOC contents (from 0.57 to 1.34 wt.%), with TIC contents of 0.13 to 0.99 wt.%, and $\delta^{13}C_{org}$ values of -31.8 to -30.8‰ (Fig. 3). The twelve IF samples from the lower CF have lower TOC (0.08 to 0.14 wt.%) and higher TIC (1.42 to 3.19 wt.%) contents, with $\delta^{13}C_{org}$ values that range from -29.9 to -28.1‰. The single sandstone sample from the top of the lower CF has a low TOC content (0.08

wt.%) with no detectable TIC, and a $\delta^{13}C_{org}$ value of -28.8‰. The black shale samples from the upper CF have TOC contents that range from 0.11 to 4.84 wt.%, with relatively low TIC values of 0 to 7.82 wt.%, and $\delta^{13}C_{org}$ values that range from -33.4 to -29.3‰ (Fig. 3). The dolostone samples in the upper CF have relatively low TOC contents of 0.03 to 0.61 wt.%, with expected higher TIC values of 8.38 to 12.80 wt.%, and $\delta^{13}C_{org}$ values that range from -33.4 to -29.7‰.

All IF samples have low Y/Ho ratios, ranging from 23.50 to 26.05 (Fig. 3). When normalized to PAAS, the IF samples show depletions in light REEs (LREEs) and enrichments in heavy REEs (HREEs; exemplified by PAAS-normalized ratios of Pr to Yb, where Pr_{PAAS}/Yb_{PAAS} ratios range from 0.35–0.76; Appendix B; Bau et al., 1996; Planavsky et al., 2010). Slight positive Eu anomalies ($Eu/Eu^* = 1.14–1.47$; where $Eu/Eu^* = Eu_{PAAS}/(0.67\times Sm_{PAAS} + 0.33\times Tb_{PAAS})$) and no true Ce anomalies (based on a Ce/Ce^* versus Pr/Pr^* plot) are evident (Appendix A; Fig. 3). Dolostone also lack true Ce anomalies (Appendix A). The black shale and dolostone samples throughout the CF have weakly positive Eu anomalies ($Eu/Eu^* = 1.00–1.31$, with the exception of one dolostone sample towards the top of the CF, which has a slightly negative Eu/Eu^* anomaly of 0.96).

The IF samples have high Fe_T concentrations, ranging from 45.6 to 59.9 wt.% (Appendix B), with very high Fe_T/Al ratios of 27.6–61.4 (Fig. 4). The shale samples have variable Fe_T concentrations and Fe_T/Al ratios of 1.06–36.1 wt.% and 0.11–44.4, respectively. Dolostone samples have low Fe_T concentrations of 1.16–3.22 wt.%, and Fe_T/Al ratios ranging from 0.76 to 10.9. Most of our samples have high Fe_{HR}/Fe_T ratios (> 0.38; n = 98; Fig. 4). However, 4 samples have low Fe_{HR}/Fe_T ratios (< 0.22), and 30 samples have Fe_{HR}/Fe_T ratios ranging from 0.22 to 0.38, and these samples tend to cluster around depth intervals 381.1–401.9 m and 420.5–484.8 m. All of the samples have very low Fe_{py}/Fe_{HR} ratios (< 0.11; Fig. 4). IFs have consistently elevated RSE (U, Mo and V) concentrations when normalized to Al (Fig. 4). By contrast, other samples (particularly the shales) have variable U/Al, Mo/Al and V/Al ratios (Fig. 4).

In the lower CF, all IF samples have slightly positive $\delta^{56}Fe$ values (0.05 to 0.35‰, average = 0.19 ± 0.09‰; Fig. 4). The $\delta^{56}Fe$ value of the single sandstone sample is -0.44‰. The 4 black shale samples have $\delta^{56}Fe$ values ranging from -0.10 to 0.32‰ (average = 0.15 ± 0.14‰). In the upper CF, the $\delta^{56}Fe$ values of black shales spread across a large range, from -0.60 to 0.54‰ (0.08‰ ± 0.29‰, n = 13), and the dolostones have slightly negative $\delta^{56}Fe$ values, ranging from -0.42 to -0.06‰ (-0.26 ± 0.11‰, n =

9; Fig. 4).

6. Discussion

6.1 Evaluating ocean redox chemistry

Our samples, which include sandstone, IF, black shale (including siderite-rich shale) and dolostone, span a significant range in water depth (from shallow through to deeper environments on the outer shelf; Fig. 2h), thus allowing a detailed reconstruction of oceanic redox structure. The IF is hosted in the lower CF, which reflects deposition in shallow intertidal to subtidal environments above fair-weather wave base (Li et al., 2015; Lin et al., 2019) (Fig. 2h). The IF samples are dominated by hematite with minor detrital phases (Figs. 2c and e), and the observed LREE depletion over HREE enrichment is similar to ancient IFs and modern seawater (Planavsky et al., 2010 and references therein). In addition, no obvious covariation is observed between Al vs. Y/Ho or Ce/Ce* ratios, suggesting that the IFs preserve primary seawater REE+Y signals without significant detrital influence (Supplementary Information Appendix A).

The absence of true negative Ce anomalies suggests that the CF IF was deposited under anoxic or dysoxic conditions. The CF IF has homogeneous low Y/Ho ratios (24–26; lower than that of upper crustal rocks and chondrite; Fig. 3), which are consistent with CF IFs from other sites in the NCC (e.g., Lin et al., 2019), and similar REE+Y features are recorded by other late Paleoproterozoic IFs (e.g., Planavsky et al., 2010; Qiu et al., 2022). Redox-induced changes in REE+Y patterns in some modern redox-stratified basins can be linked directly to Mn cycling, giving decreased Y/Ho ratios below the Mn chemocline (Planavsky et al., 2010). Oxidation of Mn(II) to Mn(IV) requires a higher redox potential compared to Fe(II) and takes place above the Fe chemocline (e.g., Tebo et al., 2004; Ossa Ossa et al., 2018). Therefore, like some late Paleoproterozoic IFs, the low Y/Ho ratios provide evidence for a shallow Mn chemocline above the Fe chemocline, where IF deposition and Mn-(oxyhydr)oxide reduction occurred. The high Fe_T/Al and Fe_{HR}/Fe_T ratios for the CF IF (Fig. 4) thus support upwelling of deeper anoxic ferruginous waters to the Fe chemocline. The enrichments in U, Mo and V (see discussion below for the evaluation of local redox thresholds) in IF samples either reflects anoxic water column conditions, at least around the sediment-water interface, or uptake and draw down in association with Fe minerals that precipitated at the Fe chemocline (see below).

The non-IF samples with elevated Fe_{HR}/Fe_T (>0.38) and Fe_T/Al ratios (>0.55 ±

0.11), as well as low Fe_{py}/Fe_{HR} ratios (Fig. 4), suggest that anoxic and ferruginous water column conditions were a prevalent feature during deposition of the CF. However, the low Fe_T/Al and Fe_{HR}/Fe_T ratios for non-IF samples in the lower CF, as well as groupings of samples in the upper CF, suggest oxic or equivocal deposition (Fig. 4). In terms of the upper CF, these samples occur from 381.1–401.9 m and 420.5–484.8 m, and are interspersed with samples that have elevated Fe_T/Al and Fe_{HR}/Fe_T ratios, suggesting that the water column likely fluctuated between oxic and anoxic-ferruginous conditions through these zones. However, to provide a more robust redox evaluation, we consider these Fe speciation data alongside our redox sensitive trace element data.

Uranium is particularly useful in this context because U and Fe have similar redox potentials, and both require only water column anoxia (i.e., not sulfide) to generate significant enrichments (e.g., Anderson et al., 1989; Poulton, 2021). Here, recognising that redox proxy thresholds should be characterised for the local environment wherever possible (e.g., Poulton, 2021) we take the approach of recent studies (e.g., Li et al., 2023) and consider U and Fe systematics together (Fig. 5a). This approach demonstrates that U/Al ratios only start to increase when Fe_{HR}/Fe_T ratios approach ~0.45, suggesting that samples below this value were likely deposited under oxic conditions. Some of the samples with Fe_{HR}/Fe_T ratios >0.45 also have relatively low U/Al ratios, but we note here that elevated U/Al ratios coincident with high Fe_{HR}/Fe_T ratios is also a characteristic of anoxic ferruginous waters upwelling into oxic shallower waters, and thus these sporadic samples likely represent deeper water anoxia. Thus, taking these considerations together, we utilise samples with Fe_{HR}/Fe_T ratios of <0.45 to provide oxic baseline ranges for U/Al (0.22 ± 0.41), Mo/Al (0.19 ± 0.48) and V/Al (9.52 ± 2.49), and we use this redox calibration to distinguish dominantly oxic and ferruginous samples on the trace element plots (Fig. 4).

Our local redox calibration supports fluctuating water column redox conditions, from oxic to anoxic, on a variety of timescales through the CF (Fig. 4). Intervals of anoxic deposition are supported by elevated U/Al and V/Al ratios, alongside high Fe_T/Al and Fe_{HR}/Fe_T ratios, while the very low Fe_{py}/Fe_{HR} ratios in these well-preserved drill core samples suggests ferruginous anoxia. Given this interpretation, the moderate enrichments that occur in Mo/Al ratios in dominantly ferruginous intervals likely reflect Mo draw down via uptake to Fe minerals formed in the ferruginous water column (the ‘particle shuttle’ mechanism; Tribovillard et al., 2006). We note here that anoxic intervals occur in both black shale and dolostone intervals (Fig. 4), and dolostones also lack Ce anomalies, suggesting that there is no specific lithological control on the redox interpretation. Indeed, since the dolostones likely formed in shallower waters relative to the black shale, a major deepening of the oxycline at certain intervals appears likely. Thus, in contrast to the shallow oxycline invoked for the lower CF (above fair weather wave base, which is usually <20 m in modern settings), redox fluctuations in the upper CF resulted in the periodic oxygenation of deeper waters (likely below storm wave base, which may be up to 200 m). Previous studies of the CF at other sites also show highly variable Fe speciation characteristics (Fig. 5b; Planavsky et al., 2011; Li et al., 2015), providing support for fluctuations in the depth of water column oxygenation at the end of Paleoproterozoic era.

6.2 Iron cycling and generation of the Chuanlinggou IF

Iron formations are rare between 1.8 and 0.8 Ga (e.g., Bekker et al., 2010), and therefore, the formation of the Chuanlinggou IF at ~1.64 Ga likely required a source of Fe(II) well in excess of the normal mid-Proterozoic marine flux. Recent studies have provided support for a strong hydrothermal flux at this time (Lin et al., 2019), and since the CF coincides with the breakup of Columbia (Kusky and Li, 2003; Lin et al., 2019), increased hydrothermal activity would be expected. Indeed, both the CF IF samples and the overlying sediments of the upper CF have positive Eu anomalies (Fig. 3), which are widely considered to define hydrothermal inputs to the depositional setting (e.g., Bau et al., 1996). These Eu anomalies are, however, relatively small ($Eu/Eu^* = 1.14–1.47$; Fig. 3), and follow a general trend of reduced Eu anomalies through time, from IFs deposited in the Archean Eon ($Eu/Eu^* = 1.2−4.5$) to the Neoproterozoic era ($Eu/Eu^* = 1−1.4$) (Konhauser et al., 2017). Nevertheless, the presence of positive Eu anomalies in almost all of the CF samples strongly points to a hydrothermal signature. Since submarine hydrothermal activity commonly supplies Fe(II) to the marine environment, elevated Fe concentrations linked to enhanced hydrothermal activity likely played a major role in the genesis of the Chuanlinggou IF (Lin et al., 2019), although we stress that this would likely have been in addition to Fe(II) supplied via release from sediment porewaters under widespread ferruginous conditions (Poulton and Canfield, 2011; Poulton, 2021).

The continuation of small positive Eu anomalies in the upper CF also has implications for the continued persistence of deeper ferruginous waters after deposition of the IF. Previous studies have argued that the flux of organic matter was a major control on the redox landscape of the mid-Proterozoic ocean, with productivity and the organic flux limiting the extent of euxinia (Planavsky et al., 2011). Generally low TOC contents in the CF (average = 0.66 ± 0.77 wt.%) might be consistent with this view. However, some samples have higher TOC contents (up to 4.8 wt.%; Fig. 3), and yet do not show evidence for enhanced sulfide production, even during diagenesis (as indicated by very low pyrite concentrations). Relative changes in the oceanic influx of Fe_{HR} and sulfate have also been proposed as a first-order control on the chemical nature of water column anoxia in the mid-Proterozoic (Poulton and Canfield, 2011). An enhanced hydrothermally-derived supply of dissolved Fe(II) would provide a specific mechanism to increase the upwelling flux of dissolved Fe(II), thereby ultimately increasing the flux of Fe_{HR} (after precipitation in the water column) relative to sulfate. We therefore suggest that a significant supply of hydrothermally-derived Fe(II) provided a source for the Chuanlinggou IF, as well as subsequently helping to maintain ferruginous deeper water column conditions through the upper CF.

The IF samples in the CF have positive $\delta^{56}Fe_{HR}$ values (0.04–0.42‰, average = 0.21 ± 0.12‰) which is higher than expected for the hydrothermal flux (-0.5 to 0.0‰; Johnson et al., 2008; Planavsky et al., 2012), and also higher than values expected during the reductive dissolution of Fe (oxyhydr)oxides during diagenesis (-2.5 to -0.5‰; Johnson et al., 2008; Ossa Ossa et al., 2018). Hence, partial oxidation of Fe(II) is a likely explanation for the Fe isotopic composition of our IF samples (e.g., Bekker et al., 2010). Importantly, there is a weak negative correlation between $\delta^{56}Fe$ and Fe_T/Al ($R^2 = 0.33$) and a strong negative correlation between $\delta^{56}Fe_{HR}$ and Mn/Fe ($R^2 = 0.82$) (Figs. 6a and b), which suggests that the Fe isotopic compositions of the IFs may be influenced by the formation of Fe carbonate phases (e.g., siderite and ankerite; Fe_{carb}) and limited detrital minerals, consistent with petrological observations and Fe speciation results (Appendix A). The oxidizing mechanism involved in this partial oxidation is difficult to define based on Fe isotopes. Previous studies have suggested microbial oxidation of Fe(II) by microaerophilic FeOB (Lin et al., 2019; and references therein), which thrive under dysoxic conditions. However, anoxygenic photosynthesizers may also have oxidized the Fe(II) (Bekker et al., 2010). The average $\delta^{13}C_{org}$ values for the IFs (about -29‰), likely reflect photoautotrophic CO_2 fixation as the dominant primary producers (e.g., Ossa Ossa et al., 2019; Rego et al., 2021). Overall, our results suggest that microaerophilic FeOB and/or anoxygenic photosynthesizers exerted the main control on the deposition of the CF IFs (Fig. 7a).

The dolostones have slightly negative $\delta^{56}Fe_{HR}$ values, ranging from -0.53 to -0.11‰ (average of -0.34 ± 0.15‰), and $\delta^{56}Fe$ values exhibit a weak negative correlation with Fe_T/Al (R^2 = 0.33, Fig. 6a). Since Fe isotope fractionations between Fe-carbonate phases and $Fe(II)_{aq}$ range between -0.2 and -0.7‰ (e.g., Wiesli et al., 2004; Rego et al., 2021), this suggests that the dolostone may have formed in equilibrium with seawater ($\delta^{56}Fe$=0‰, Johnson et al., 2008), although the presence of minor detrital minerals may have resulted in increased $\delta^{56}Fe_{HR}$ values in some dolostone samples.

The DIR process would have created an isotopically light Fe pool in porewaters, relative to the initial Fe-(oxyhydr)oxide minerals (Planavsky et al., 2012; Ossa Ossa et al., 2018). However, complete Fe reduction would produce early diagenetic minerals with a similar Fe isotope composition to the precursor Fe-(oxyhydr)oxides (Johnson et al., 2008). For the black shales, the Fe isotope values of the Fe_{HR} fraction range from -2.57 to 1.09‰. These shale samples can be divided into three groups. Firstly, two samples have $\delta^{56}Fe_{HR}$ -2.57 and -1.31‰, and these samples are dominated Fe_{carb}. Combined with negative $\delta^{13}C_{carb}$ values (-3.4 ± 1.4‰) in the CF black shales, this supports diagenetic carbonate precipitation (Li et al., 2015) following DIR. Secondly, 8 black shale samples (which is dominated by Fe_{carb}, with minor Fe_{mag}) have $\delta^{56}Fe_{HR}$ values ranging from -0.66 to -0.16‰, and one siderite-rich shale sample has a $\delta^{56}Fe_{HR}$ value of -0.60‰. These values can be explained by a balance between the formation of Fe carbonate minerals and magnetite. For the third group, the $\delta^{56}Fe_{HR}$ values of black shales range from 0.53 to 1.43‰ (n = 6), and is dominated by Fe carbonate phases and magnetite. In addition, the $\delta^{56}Fe$ values show a positive correlation with Fe_T/Al (R^2 = 0.46, Fig. 6c), but no correlation between $\delta^{56}Fe_{HR}$ and Mn/Fe (Fig. 6d). These data can be attributed to mixing between Fe(II) formed from near complete DIR, which would inherit the initial positive $\delta^{56}Fe$ values of Fe-(oxyhydr)oxides, and an overprint from detrital materials. For example, sample 6-78 has a $\delta^{56}Fe$ value of 0.15, which is close to crustal values, and also has a low Fe_{HR}/Fe_T ratio of 0.18, supporting a dominant signature from detrital minerals. Therefore, we conclude that mixing between different Fe mineral phases can explain the $\delta^{56}Fe$ variability (Fig. 7b).

The $\delta^{13}C_{org}$ composition ranges from -33.4 to -28.1‰, dependent on sedimentary facies (Luo et al., 2014), where the $\delta^{13}C_{org}$ composition of shallower water sediments is generally ^{13}C-enriched relative to deeper water sediments. Average $\delta^{13}C_{org}$ values of about -29‰ for shallow water sediments (IFs and sandstone) likely reflect a kinetic isotope fractionation produced by autotrophic organisms (Schidlowski, 2001), which initiated deposition of the CF IF. By contrast, the deeper-water $\delta^{13}C_{org}$ values may reflect biological carbon cycling (e.g., Ossa Ossa et al., 2019), potentially with a significant contribution from dissimilatory Fe reducers, as Fe in carbonate phases (i.e., Fe_{carb}) is common in these sediments. Hence, the water column appears to have been both redox and ecologically stratified, with autotrophic organisms (microaerophilic FeOB and/or anoxygenic photosynthesizers) in shallower waters, and dissimilatory Fe reducers driving Fe reduction in deeper waters (Figs. 7a and b).

6.3 Implications for biological evolution during the mid-Proterozoic

As discussed above, the deeper ocean was dominated by anoxic and ferruginous conditions, with pulses of water column oxygenation at 1.57–1.56 Ga (e.g., Zhang et al., 2018; Luo et al., 2021), ~1.4 Ga (Zhang et al., 2016) and ~1.33 Ga (Canfield et al., 2018a) (Fig. 8a). Our data extend these fluctuations back to the late Proterozoic, suggesting that episodic deeper water oxygenation (likely extending to outer shelf settings) was a common phenomenon between the GOE and NOE. The oxygen levels required for early animal respiration were lower than those needed to sustain large motile animals (Canfield et al., 2018a). For example, an oxygen requirement of around 0.1–0.2% PAL is typical for a choanoflagellate with a diameter of 5–10 μm, and 0.36% PAL has been calculated as the requirement for small bilaterian animals (Canfield et al., 2018a). Eukaryotic life had likely evolved at least by the late Paleoproterozoic era (e.g., Zhu et al., 2016), and our data reinforce the suggestion that sufficient levels of oxygen for animal evolution were episodically available. Thus, it appears that highly fluctuating redox conditions likely constrained the radiation of eukaryotes, and by extension the ultimate rise of animals (e.g., Luo et al., 2021).

7. Conclusions

Our new geochemical data for the ~1.64 Ga Chuanlinggou Formation provides support for a redox-stratified ocean with oxic surface waters overlying ferruginous deeper waters. However, the data also provide insight into the intensity and dynamics of ferruginous conditions during the Late Paleoproterozoic. In this context, the general lack of IFs between ~1.88 Ga and the Cryogenian is commonly considered to represent decreased dissolved Fe(II) concentrations relative to the Archean and earlier intervals of the Paleoproterozoic (e.g., Song et al., 2018). The Chuanlinggou IF contrasts with this broader scale outlook, representing an extensive deposit that formed in a shallow ocean setting during an interval of particularly elevated Fe concentrations. This interval of more intense ferruginous conditions was likely a consequence of hydrothermal activity during the breakup of the Columbia supercontinent, and autotrophic Fe-oxidizers likely played a key role in the precipitation of the Fe minerals that comprise the IF.

The Chuanlinggou IF adds to a growing database of mid-Proterozoic IFs from different locations, including central Arizona in the USA, the Xiamaling and Yunmenshan IFs of the NCC, and the Jingtieshan IF in North Qilian, northwestern China (Fig. 8b; Bekker et al., 2010; Yang et al., 2015; Canfield et al., 2018b; Qiu et al., 2022). Most of these IFs have significant hydrothermal signals (e.g., Yang et al., 2015; Canfield et al., 2018b), suggesting that intervals of enhanced hydrothermal activity played an important role in their genesis. Thus, dissolved Fe(II) concentrations were likely highly dynamic across the mid-Proterozoic, and in large part this appears to have been a consequence of tectonic activity (Fig. 8c). Data for shales that overly the Chuanlinggou IF additionally suggest episodic intervals of deeper water oxygenation. Thus, similar to recent studies of the later Mesoproterozoic ocean, our data indicate that ocean oxygenation during the latest Paleoproterozoic may have been more dynamic than previously considered. These fluctuating levels of oxygenation may have served as a constraint on the early evolution of eukaryotes.

CRediT authorship contribution statement

Xiuqing Yang: Data collection, Investigation, Visualization, Writing – original draft. **Jingwen Mao**: Supervision, Writing – review & editing. **Rongxi Li**: Supervision, Writing-review & editing. **Fang Huang**: Data analysis, Writing – review & editing. **Chong He**: Resources, Data analysis. **Chao Zhao**: Visualization, Writing – review & editing. **Wei Wei**: Data analysis, Writing – review & editing. **Guowei Yang**: Investigation. **Yijun Xiong**: Data analysis. **Simon W. Poulton**: Conceptualization, Writing – review & editing.

Declaration of competing interest

The authors declare that they have no competing financial interests or personal relationships that could have appeared to influence the work reported in this paper.

Acknowledgements

Support for this project was provided by the National Natural Science Foundation of China (No. 41972075), National Key Research and Development Program of China (2021YFA0718200) and the Fundamental Research Funds for the Central Universities, CHD (No. 300102272203). We thank Tianchen He, Zhihui An, Zidong Peng and Sen Li for valuable discussion and constructive comments. We are also grateful to Huimin Yu and Sen Li for their help with iron isotope and iron speciation analyses, and Yongsheng Liang, Yun Yang, Xusheng Zhang and Hui Ma for assistance with field work. We are grateful to three anonymous reviewers and Associate Editor Huiming Bao for constructive comments that significantly improved the manuscript.

References

Alcott, L.J, Mills, B.J.W., Poulton, S.M., 2019. Stepwise Earth oxygenation is an inherent property of global biogeochemical cycling. Science 366, 1333–1337.

Anderson, R.F., Lehuray, A.P., Fleisher, M.Q., Murray, J.W., 1989. Uranium deposition in Saanich Inlet sediments, Vancouver Island. Geochim. Cosmochim. Acta 53, 2205–2213.

Bau, M., Koschinsky, A., Dulski P., Hein, J.R., 1996. Comparison of the partitioning behaviours of yttrium, rare earth elements, and titanium between hydrogenetic marine ferromanganese crusts and seawater. Geochim. Cosmochim. Acta 60(10), 1709–1725.

Bekker, A., Slack, J.F., Planavsky, A., Krapež, B., Hofmann, A., Konhauser, K.O., Rouxel, O.J., 2010. Iron formation: The sedimentary product of a complex interplay among mantle, tectonic, oceanic, and biospheric processes. Econ. Geol., 105, 467–508.

Byrne, R., Sholkovitz, E., 1996. Marine chemistry and geochemistry of the lanthanides. In Handbook on the Physics and Chemistry of the Rare Earths (eds. K. A. Gschneider Jr. and L. Eyring). Elsevier, Amsterdam.

Canfield, D.E., Raiswell, R., Westrich, J.T., Reaves, C.M., Berner, R.A., 1986. The use of chromium reduction in the analysis of reduced inorganic sulfur in sediments and shales. Chem. Geol. 54, 149–155.

Canfield, D.E, Zhang, S., Frank, A.B., Wang, X., Wang, H., Su, J., Ye, Y., Frei, R., 2018a. Highly fractionated chromium isotopes in Mesoproterozoic-aged shales and atmospheric oxygen. Nat. Comms. 9, 2871.

Canfield, D.E., Zhang, S., Wang, H., Wang, X., Zhao, W., Su, J., Bjerrum, C.J., Haxen, E.R., Hammarlund, E., 2018b. A Mesoproterozoic iron formation. Proc. Natl. Acad. Sci. USA 115(17), 3895–3904.

Clarkson, M.O., Poulton, S.W., Guilbaud, R., Wood, R.A., 2014. Assessing the utility of Fe/Al and Fe-speciation to record water column redox conditions in carbonate-rich sediments. Chem. Geol. 382, 111–122.

Emerson, S.R., Huested, S.S., 1991, Ocean anoxia and the concentrations of molybdenum and vanadium in seawater. Mar. Chem. 34, 177–196.

Gumsley, A.P., Chamberlain, K.R., Bleeker, W., Söderlund, U., de Kock, M.O., Larsson, E. M., Bekker, A., 2017.Timing and tempo of the Great Oxidation Event. Proc. Natl Acad. Sci. USA 114, 1811–1816.

Helz, G.R., Miller, C. V., Charnock, J.M., Mosselmans, J.F.W., Pattrick, R.A.D., Garner, C.D., Vaughan, D.J., 1996. Mechanism of molybdenum removal from the sea and its concentration in black shales: EXAFS evidence. Geochim. Cosmochim. Acta 60, 3631–3642.

Holland, H., 1984. The chemical evolution of the atmosphere and oceans. New York, Princeton University Press, 582 p.

Huang, F., Zhang, Z., Lundstrom, C.C., Zhi X., 2011. Iron and magnesium isotopic compositions of peridotite xenoliths from Eastern China. Geochim. Cosmochim. Acta, 75(12), 3318–3334.

Johnson, C.M., Beard, B.L., Klein, C., Beukes, N.J., Roden, E.E., 2008. Iron isotopes constrain biologic and abiologic processes in banded iron formation genesis. Geochim. Cosmochim. Acta 72, 151–169.

Konhauser, K.O., Planavsky, N.J., Hardisty, D.S., Robbins, L.J., Warchola, T.J., Haugaard, R., Lalonde, S.V., Partin, C.A., Oonk, P.B.H., Tsikos, H., Lyons, T.W., Bekker, A., Johnson, C.M., 2017. Iron formations: a global record of Neoarchaean to Palaeoproterozoic environmental history. Earth-Sci. Rev. 172, 140–177.

Krause AJ, Mills BJW, Zhang S, Planavsky NJ, Lenton TM, Poulton SW. 2018. Stepwise oxygenation of the Paleozoic atmosphere. Nature Comms. 9, 4081.

Krause, A.J., Mills, B.J.W., Merdith, A.S., Lenton, T.M., Poulton, S.W., 2022. Extreme variability in atmospheric oxygen levels in the late Precambrian. Sci. Adv., 8, eabm8191.

Kusky, T.M., Li, J., 2003. Paleoproterozoic tectonic evolution of the North China Craton. J. Asian Earth Sci. 22(4), 383–397.

Li, C., Planavsky, N.J., Love, G.D., Reinhard, C.T., Hardisty, D., Feng, L., Bates, S.M., Huang, J., Zhang, Q., Chu, X., 2015. Marine redox conditions in the middle Proterozoic ocean and isotopic constraints on authigenic carbonate formation: Insights from the Chuanlinggou Formation, Yanshan Basin, North China. Geochim. Cosmochim. Acta 150, 90–105.

Li, S., Wignall, P.B., Xiong, Y.J., Poulton, S.W., 2023. Calibration of redox thresholds in black shale: Insight from a stratified Mississippian basin with warm saline bottom waters. Geol. Soc. Am. Bull. 21, 10.1130/B36915.1.

Lin, Y., Tang, D., Shi, X., Zhou, X., Huang, K., 2019. Shallow-marine ironstones formed by microaerophilic iron-oxidizing bacteria in terminal Paleoproterozoic. Gondwana Res. 76, 1–18.

Luo, G.M., Junium, C.K., Kump, L.R., Huang, J.H., Li, C., Feng, Q.L., Shi, X.Y., Bai, X., Xie, S.C., 2014. Shallow stratification prevailed for 1700 to 1300 Ma ocean: evidence from organic carbon isotopes in the North China Craton. Earth Planet. Sci. Lett. 400, 219–232.

Luo, J., Long, X., Bowyer, F.T., Mills, B., Li, J., Xiong, Y.K., Zhu, X.K., Zhang, K., Poulton, S.W., 2021. Pulsed oxygenation events drove progressive oxygenation of the early Mesoproterozoic ocean. Earth Planet. Sci. Lett. 559, 116754.

Lyons, T.W., Reinhard, C.T., Planavsky, N.J., 2014. The rise of oxygen in earth's early ocean and atmosphere. Nature 506, 307-315.

Ossa Ossa, F., Hofmann, A., Wille, M., Spangenberg, J.E., Bekker, A., Poulton, S. W., Schoenberg, R., 2018. Aerobic iron and manganese cycling in a redox-stratified Mesoarchean epicontinental sea. Earth Planet. Sci. Lett. 500, 28–40.

Ossa Ossa, F., Hofmannn, A., Spangenberg, J.E., Poulton, S.W., Stüeken, E.E., Schoenberg, R., Eickman, B., Wille, M., Bekker, A., 2019. Limited oxygen production in the Mesoarchean ocean. Proc. Nat. Acad. Sci. 116, 6647-6652.

Ossa Ossa, F., Spangenberg, J.E., Bekker, A., König, S., Stüeken, E. E., Hofmann, A., Poulton, S.W., Yierpan, A., Varas-Reus, M.I., Eickmann, B., Andersen, M.B., Schoenberg, R., 2022. Moderate levels of oxygenation during the late stage of Earth's Great Oxidation Event. Earth Planet. Sci. Lett. 594, 117716.

Ostrander, C.M., Nielsen, S.G., Owens, J.D., Kendall, B., Gordon, G.W., Romaniello, G. R., Anbar, A.D., 2019. Fully oxygenated water columns over continental shelves before the Great Oxidation Event. Nat. Geosci.12, 186–91.

Planavsky, N., Rouxel, O.J., Bekker, A., Hofmann, A., Little, C.T.S., Lyons, T.W., 2012, Iron isotope composition of some Archean and Proterozoic iron formations.

Geochim. Cosmochim. Acta 80, 158–169.

Planavsky, N.J., Bekker, A., Rouxel, O.J., Kamber, B., Hofmann, A., Knudsen, A., Lyons, T.W., 2010. Rare Earth Element and yttrium compositions of Archean and Paleoproterozoic Fe formations revisited: new perspectives on the significance and mechanisms of deposition. Geochim. Cosmochim. Acta 74, 6387–6405.

Planavsky, N.J., McGoldrick, P., Scott, C.T., Li, C., Reinhard, C.T., Kelly, A.E., Chu, X.L., Bekker, A., Love, G.D., Lyons, T.W., 2011. Widespread iron-rich conditions in the mid-Proterozoic ocean. Nature 477, 448–495.

Poulton, S.W., 2021. The Iron Speciation Paleoredox Proxy: Elements in Geochemical Tracers in Earth System Science. Cambridge University Press.

Poulton, S.W., Bekker, A., Cumming, V.M., Zerkle, A.L., Canfield. D.E., Johnston, D.T., 2021. A 200-million-year delay in permanent atmospheric oxygenation. Nature 592, 232–236.

Poulton, S.W., Canfield, D.E., 2005. Development of a sequential extraction procedure for iron: implications for iron partitioning in continentally derived particulates. Chem. Geol. 214, 209–221.

Poulton, S.W., Canfield, D.E., 2011. Ferruginous conditions: a dominant feature of the ocean through Earth's history. Elements 7, 107–112.

Qiu, Y., Qin, L., Huang, F., Zhao, T., Li, Y., 2022. Early prosperity of iron bacteria at the end of the Paleoproterozoic era. Geophys. Res. Lett. 49, e2022GL097877.

Rego, E.S., Busigny, V., Lalonde, S.V., Philippot, P., Bouyon, A., Rossignol, C., Babinski, M., Zapparoli, A.C., 2021. Anoxygenic photosynthesis linked to neoarchean iron formations in carajás (Brazil). Geobiology 19, 326–341.

Schidlowski, M., 2001. Carbon isotopes as biogeochemical recorders of life over 3.8 Ga of earth history: Evolution of a concept. Precambrian Res. 106, 117–134.

Song, H., Jiang, G., Poulton S.W., Wignall P.B., Wang, C., 2017. The onset of widespread marine red beds and the evolution of ferruginous oceans. Nat. Comms. 8, 399.

Song Y., Bowyer F.T., Mills B.J.W., Merdith A.S., Wignall P.B., Peakall J., Zhang S., Wang X., Wang H., Canfield D.E., Shields G.A., Poulton S.W. (2023) Dynamic redox and nutrient cycling response to climate forcing in the Mesoproterozoic ocean. Nature Comms. 14, 6640.

Tebo, B.M., Bargar, J.R., Clement, B.G., Dick, G.J., Murray, K.J., Parker, D., Verity, R., Webb, S.M., 2004. Biogenic manganese oxides: properties and mechanisms of formation. Annu. Rev. Earth Planet. Sci. 32, 287–328.

Tribovillard, N., Algeo, T.J., Lyons, T., Riboulleau, A., 2006. Trace metals as paleoredox and paleoproductivity proxies: an update. Chem. Geol. 232, 12–32.

Wiesli, R.A., Beard, B.L., Johnson, C.M., 2004. Experimental determination of Fe isotope fractionation between aqueous Fe(II), siderite and "green rust" in abiotic systems. Chem. Geol. 211, 343–362.

Yang, X.Q., Zhang, Z.H., Duan, S.G., Zhao, X.M., 2015. Petrological and geochemical features of the Jingtieshan banded iron formation (BIF): a unique type of BIF from the Northern Qilian Orogenic Belt, NW China. J. Asian Earth Sci. 113, 1218–1234.

Zahnle, K., Claire, M.W., Catling, D., 2006. The loss of mass-independent fractionation in sulfur due to a Palaeoproterozoic collapse of atmospheric methane. Geobiology 4, 271–283.

Zhang, K., Zhu, X., Wood, R.A., Shi, Y., Gao, Z., Poulton, S.W., 2018. Oxygenation of the Mesoproterozoic ocean and the evolution of complex eukaryotes. Nat. Geosci. 11, 345–350.

Zhang, S., Wang, X., Wang, H., Bjerrum, C.J., Hammarlund, E.U., Costa, M.M., Connelly, J.N., Zhang, B., Su, J., Canfield, D.E., 2016. Sufficient oxygen for animal respiration 1,400 million years ago. Proc. Nat. Acad. Sci. 113, 1731–1736.

Zhao, G.C., Wilde, S.A., Cawood, P.A., Sun, M., 2001. Archean blocks and their boundaries in the North China Craton: lithological, geochemical, structural and P–T path constraints and tectonic evolution. Precambrian Res. 107, 45–73.

Zhu, S., Zhu, M., Knoll, A.H., Yin, Z., Zhao, F., Sun, S., Qu, Y., Shi, M., Liu, H., 2016. Decimetre-scale multicellular eukaryotes from the 1.56-billion-year-old Gaoyuzhuang Formation in North China. Nat. Comms. 7, 11500.

Figures

Fig. 1. a. Major tectonic units in China, with the position of the North China Craton (Zhao et al., 2001); b. Geological map of the North China Craton (Canfield et al., 2018b); c. Mid-Proterozoic stratigraphic profile of the Yanliao Basin (modified after Zhu et al., 2016, with age data from references therein).

Fig. 2. a. Black shale from the upper Chuanlinggou Formation in the Xuan-Long area. b. Boundary between the upper Chuanlinggou Formation (black shale and siderite-rich shale) and the lower Chuanlinggou Formation (sandstone). c. Ooidal IF. d. Sandstone with rounded quartz clasts. e. The IF consists of iron ooids and minor rounded quartz clasts. f. Black shale. g. Dolostone. h. Schematic diagram showing facies subdivisions. d and e are backscattered electron (BSE) images; f and g were taken under transmitted light and plane-polarized light, respectively. Qtz-Quartz.

Fig. 3. Geochemical profiles for TOC, TIC, $\delta^{13}C$, Y/Ho and Eu/Eu^* through the CF in Xuan-Long area. The yellow circles represent the siderite-rich shale, and grey horizontal shading represents the fluctuating zones between oxic and anoxic-ferruginous conditions (see text for details).

Fig. 4. Geochemical profiles for Fe_T/Al, Fe speciation, $\delta^{56}Fe$ and redox sensitive elements through the CF in the Xuan-Long area. $\delta^{56}Fe_{WR}$ and $\delta^{56}Fe_{HR}$ represent the $\delta^{56}Fe$ values of whole rock and the highly reactive Fe pool, respectively. In the Fe_T/Al, U/Al, Mo/Al and V/Al plots, the vertical shading indicates the calibrated redox thresholds (see text). The yellow circles represent the siderite-rich shale, and grey horizontal shading represents the fluctuating zones between oxic and anoxic-ferruginous conditions (see text for details).

Fig. 5. a. Plots of U/Al versus Fe_{HR}/Fe_T (all data from this study). b. Fe speciation data for the Chuanlinggou Formation, with previous data from Planavsky et al. (2011) and Li et al. (2015).

Fig. 6. a. Plot of $\delta^{56}Fe$ versus Fe_T/Al for ironstone and dolostone samples. b. Plot of $\delta^{56}Fe_{HR}$ versus Mn/Fe_T for ironstone and dolostone samples. c. Plot of $\delta^{56}Fe$ versus

Fe_T/Al for black shale samples. d. Plot of $\delta^{56}Fe_{HR}$ versus Mn/Fe_T for black shale samples.

Fig. 7. Seawater redox conditions and Fe cycling during deposition of the CF. a. During deposition of the lower CF, deeper waters were anoxic and ferruginous with a very shallow chemocline. Periods of enhanced upwelling caused partial oxidation of iron below the Mn chemocline, via microaerophilic FeOB and/or anoxygenic photosynthesizers. This process led to the deposition of IFs with positive δ^{56}Fe values and low Y/Ho ratios. b. During deposition of the upper CF, the position of the oxycline fluctuated, likely to below storm wave base. Dolostone formed under anoxic conditions and in equilibrium with seawater. However, partial and complete DIR of Fe-(oxyhydr)oxides transferred Fe_{ox} into Fe_{carb} and Fe_{mag}, and input of detrital minerals resulted in a wide range of δ^{56}Fe values for black shale samples.

Fig. 8. Distribution of IFs and the redox history of the Earth. a. Evolution of atmospheric oxygen concentrations through time. The purple curve shows the classical, two-step view of atmospheric evolution, while the blue curve shows the emerging model (after Lyons et al., 2014). Blue arrows represent intervals with apparent enhanced oxygenation levels. b. Secular trend in the distribution of IFs (modified after Bekker et al., 2010, with the addition of the CF IF and others). c. Evolution of marine conditions through time. a and c were modified after Alcott et al. (2019). The dark green and light green shading represent moderate/high and low Fe concentrations, respectively.

Appendix A. Supplementary material

Appendix B. Supplementary data

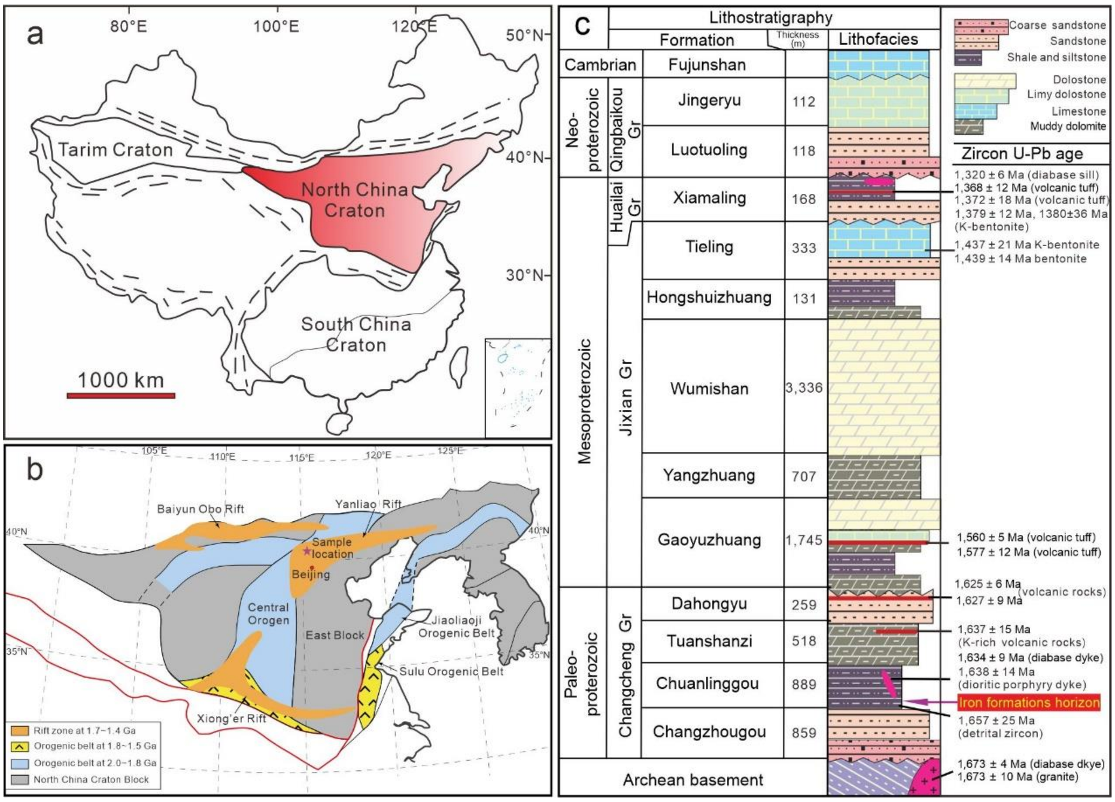

Fig. 1. a. Major tectonic units in China, with the position of the North China Craton (Zhao et al., 2001); b. Geological map of the North China Craton (Canfield et al., 2018b); c. Mid-Proterozoic stratigraphic profile of the Yanliao Basin (modified after Zhu et al., 2016, with age data from references therein).

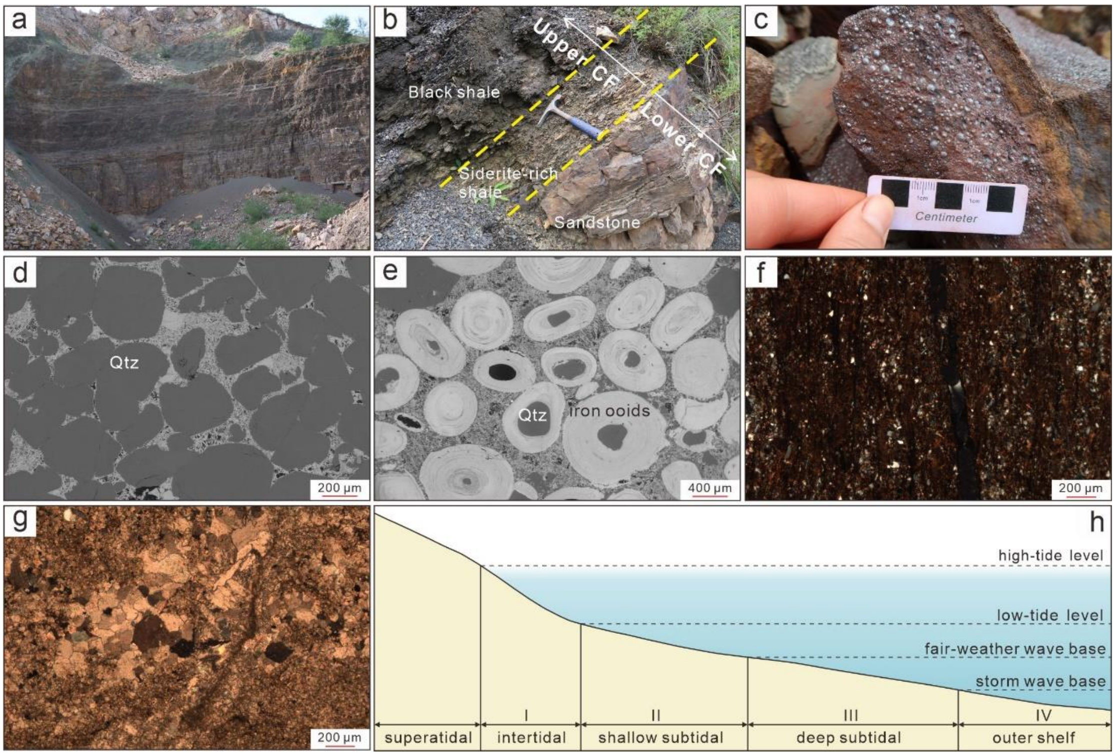

Fig. 2. a. Black shale from the upper Chuanlinggou Formation in the Xuan-Long area. b. Boundary between the upper Chuanlinggou Formation (black shale and siderite-rich shale) and the lower Chuanlinggou Formation (sandstone). c. Ooidal IF. d. Sandstone with rounded quartz clasts. e. The IF consists of iron ooids and minor rounded quartz clasts. f. Black shale. g. Dolostone. h. Schematic diagram showing facies subdivisions. d and e are backscattered electron (BSE) images; f and g were taken under transmitted light and plane-polarized light, respectively. Qtz-Quartz.

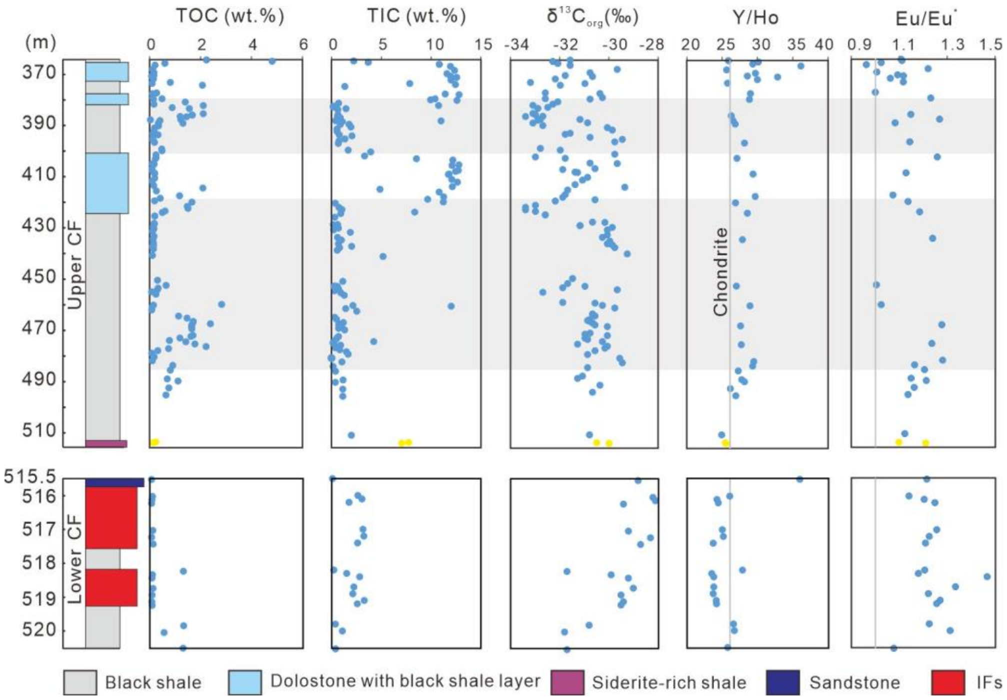

Fig. 3. Geochemical profiles for TOC, TIC, $\delta^{13}C$, Y/Ho and Eu/Eu* through the CF in Xuan-Long area. The yellow circles represent the siderite-rich shale, and grey horizontal shading represents the fluctuating zones between oxic and anoxic-ferruginous conditions (see text for details).

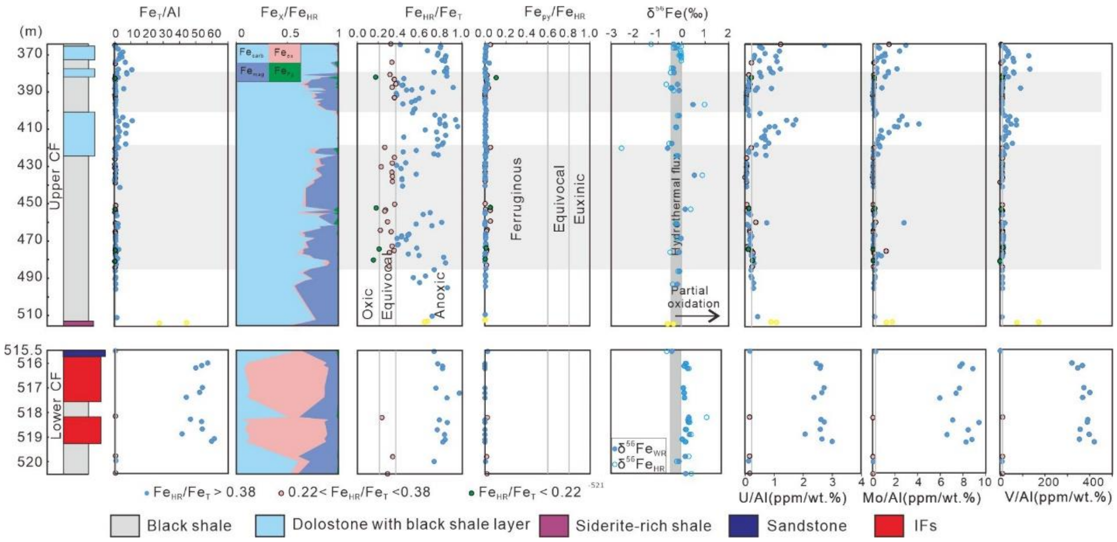

Fig. 4. Geochemical profiles for Fe_T/Al, Fe speciation, δ^{56}Fe and redox sensitive elements through the CF in the Xuan-Long area. $\delta^{56}Fe_{WR}$ and $\delta^{56}Fe_{HR}$ represent the δ^{56}Fe values of whole rock and the highly reactive Fe pool, respectively. In the Fe_T/Al, U/Al, Mo/Al and V/Al plots, the vertical shading indicates the calibrated redox thresholds (see text). The yellow circles represent the siderite-rich shale, and grey horizontal shading represents the fluctuating zones between oxic and anoxic-ferruginous conditions (see text for details).

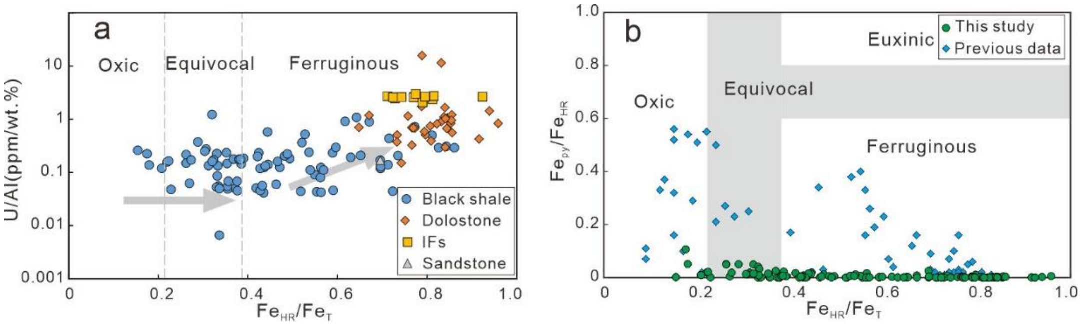

Fig. 5. a. Plots of U/Al versus Fe_{HR}/Fe_T (all data from this study). b. Fe speciation data for the Chuanlinggou Formation, with previous data from Planavsky et al. (2011) and Li et al. (2015).

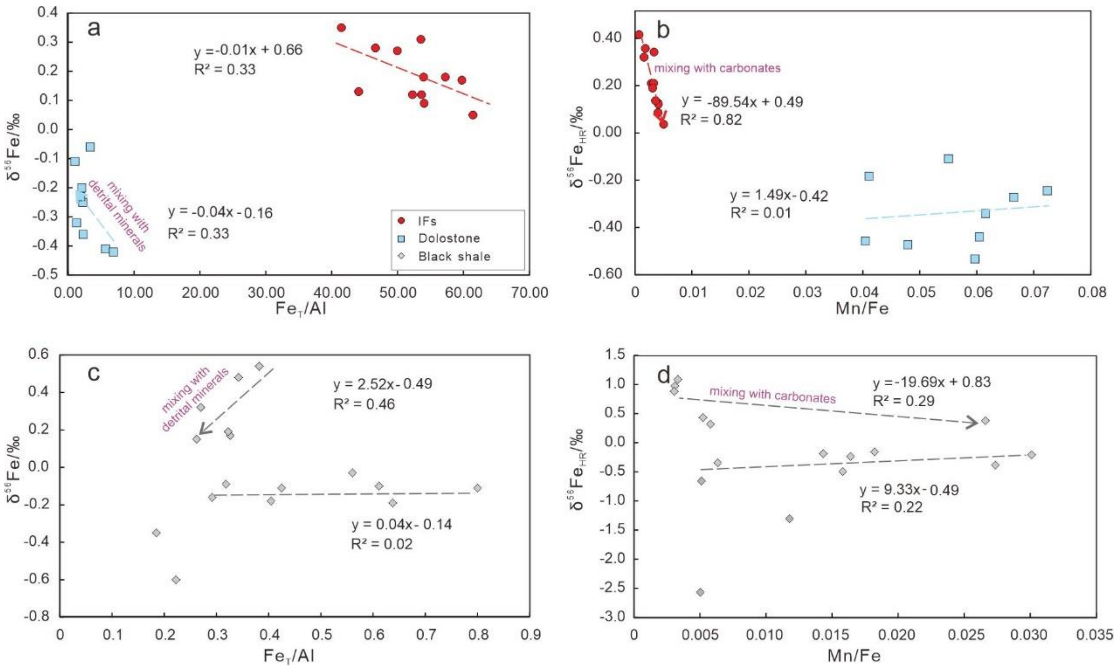

Fig. 6. a. Plot of δ^{56}Fe versus Fe_T/Al for ironstone and dolostone samples. b. Plot of $\delta^{56}Fe_{HR}$ versus Mn/Fe_T for ironstone and dolostone samples. c. Plot of δ^{56}Fe versus Fe_T/Al for black shale samples. d. Plot of $\delta^{56}Fe_{HR}$ versus Mn/Fe_T for black shale samples.

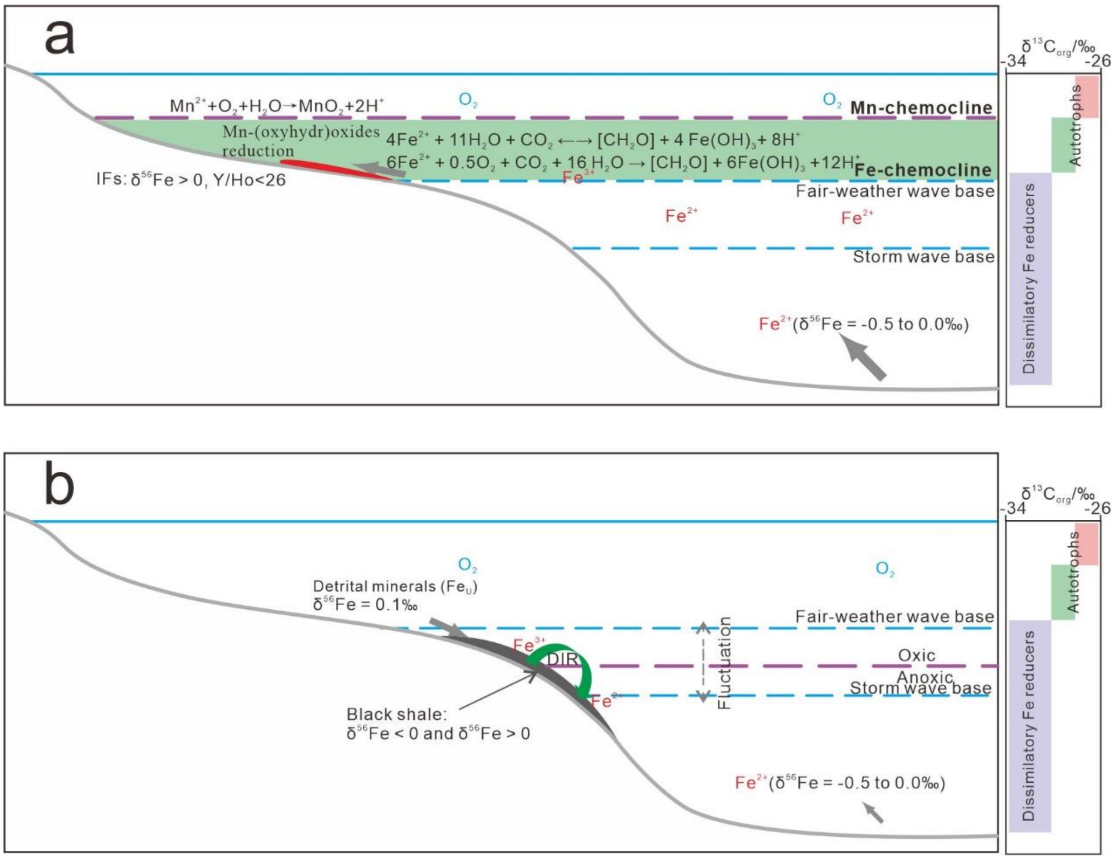

Fig. 7. Seawater redox conditions and Fe cycling during deposition of the CF. a. During deposition of the lower CF, deeper waters were anoxic and ferruginous with a very shallow chemocline. Periods of enhanced upwelling caused partial oxidation of iron below the Mn chemocline, via microaerophilic FeOB and/or anoxygenic photosynthesizers. This process led to the deposition of IFs with positive δ^{56}Fe values and low Y/Ho ratios. b. During deposition of the upper CF, the position of the oxycline fluctuated, likely to below storm wave base. Dolostone formed under anoxic conditions and in equilibrium with seawater. However, partial and complete DIR of Fe-(oxyhydr)oxides transferred Fe_{ox} into Fe_{carb} and Fe_{mag}, and input of detrital minerals resulted in a wide range of δ^{56}Fe values for black shale samples.

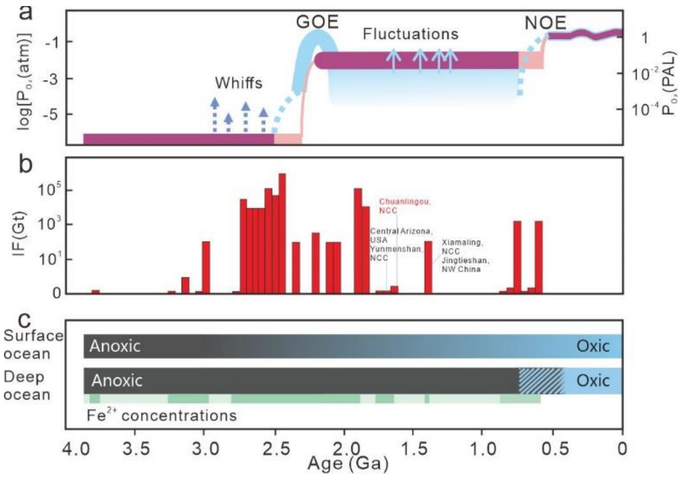

Fig. 8. Distribution of IFs and the redox history of the Earth. a. Evolution of atmospheric oxygen concentrations through time. The purple curve shows the classical, two-step view of atmospheric evolution, while the blue curve shows the emerging model (after Lyons et al., 2014). Blue arrows represent intervals with apparent enhanced oxygenation levels. b. Secular trend in the distribution of IFs (modified after Bekker et al., 2010, with the addition of the CF IF and others). c. Evolution of marine conditions through time. a and c were modified after Alcott et al. (2019). The dark green and light green shading represent moderate/high and low Fe concentrations, respectively.

Supplementary Information

1. Geochronology

A high-precision chronological framework has been established for the Chuanlinggou Formation exposed in North China Craton (NCC) in recent years. Diagenetic xenotime from fine-grained sandstones of the Chuanlinggou Formation yielded the oldest SIMS U–Pb age of 1716 ± 3 Ma, which has been suggested as a minimum age for the formation (Zhang et al., 2015). The youngest U–Pb age of 1657 ± 25 Ma comes from detrital zircons in the Jiangjiazhai and Pangjiabu regions (Duan et al., 2018). Gao et al. (2009) obtained a SHRIMP U–Pb zircon age of 1638 ± 14 Ma from a diabase, whereas Zhang et al. (2013) obtained a SHRIMP U–Pb zircon age of 1634 ± 9 Ma from a dioritic porphyrite dyke. Both the diabase and dioritic porphyrite dyke were emplaced into the Chuanlinggou Formation. Sun et al. (2013) discovered a volcanic tuff bed in the upper Chuanlinggou Formation and obtained a SHRIMP zircon U–Pb age of 1621 ± 12 Ma. In addition, Li et al. (2013) obtained granite-porphyry dike ages of 1673 ± 10 Ma and 1669 ± 20 Ma by LA-MC-ICP-MS and SHRIMP U–Pb dating methods, and these dykes are unconformably overlain by the Changzhougou Formation. Furthermore, TIMS zircon U–Pb ages of 1625 ± 6 Ma (Lu and Li, 1991) and SHRIMP U-Pb ages of 1625.9 ± 8.9 Ma (Gao et al., 2008) from the Dahongyu volcanic rocks in the Jixian area have been reported. These geochronological ages constrain Chuanlinggou Formation deposition to ~1640 Ma (Tang et al., 2015; Lin et al., 2019).

2. Materials

All samples analyzed in this paper were obtained from fresh drill core (ZK 83-6 in the Zengjiakou iron deposit, Chicheng City, Hebei Province). The Chuanlinggou Formation in the drill core is about 174 m in thickness without dip correction (from -346.5 to -520.5 m), with comfortable contacts with the underlying Changzhougou Formation and the overlying Tuanshanzi Formation. A total of 132 samples were collected, including the lower Chuanlinggou Formation interval comprising sandstone, IF and black shale, and the upper Chuanlinggou Formation comprising black shale and dolostone. The lower Chuanlinggou Formation consists mainly of silty shales with interbedded sandstones and is characterized by sedimentary structures, such as cross bedding, indicative of a shallow subtidal to intertidal origin. The upper Chuanlinggou

Formation is mainly composed of black illitic shales with clear planar bedding, suggesting a subtidal low-energy environment during deposition (below storm wave base). Some dolostone and silty beds and lenses with relatively high-energy sedimentary structures have been found locally in the top of upper Chuanlinggou Formation, suggesting episodic shoaling into an intertidal environment (Li et al., 2015; Lin et al., 2019).

The IF mainly has an ooidal texture, and iron ooids varying from 0.1 mm to 0.5 mm in diameter. The ooids are mainly spherical to ellipsoidal in shape, with some having squashed ellipsoidal and irregular dumbbell shapes. In addition, IF samples also contain rounded quartz grains (0.02 to 0.1 mm) and minor hematite, carbonate minerals and clay mineral cements in the quartz matrix. Sandstone is mainly composed of a rounded quartz matrix and hematite cement, with minor clay minerals. Black shale mainly contains clay minerals, quartz and minor carbonate minerals. Dolostone is mainly composed of dolomite with minor clay minerals.

3. Preservation of primary geochemical and isotopic signals

The ZK 83-6 drill core provides a unique opportunity to examine shallow to deeper water sedimentary facies in the Yanliao Basin. All of the samples were collected from drill core, avoiding any influence from weathering. The mid-Proterozoic strata of the NCC are well preserved and have a metamorphic grade below prehnite–pumpellyite facies (e.g., Chu et al., 2007; Luo et al., 2014). Thus, metamorphic alteration of the geochemical data is likely insignificant. Previous studies have indicated that these strata show primary iron speciation signatures (e.g., Planavsky et al., 2011; Li et al., 2015; Zhang et al., 2018). Furthermore, the Fe isotope composition of minerals is also relatively unaffected by secondary processes, including hydrothermal and high-grade metamorphism (Dauphas et al., 2017).

Although the IF samples contain quartz debris and ~1.0 wt.% Al concentrations (as a proxy for the detrital fraction), they show LREE depletion and HREE enrichment, similar to that of ancient IFs and modern seawater (Supplementary Fig. 1a) (Bau et al., 1996). Furthermore, the IF shows no correlation between Al and Y/Ho (Supplementary Fig. 2a) and Ce/Ce* (Supplementary Fig. 2b). These suggest that the IF captures the seawater signature of REE+Y, as suggest by previous studies (Li and Zhu, 2012; Lin et al., 2019). Analytical interference with barium (Ba) can create artificial positive Eu anomalies (Dulski, 1994), but there is no correlation between either Eu and Ba, or

Eu/Eu* vs Ba/Nd in this study (Supplementary Figs. 2c and d), suggesting that the positive Eu anomalies are true attributes. In addition, all analyzed samples show no correlation between Al and Eu/Eu* (Supplementary Fig. 2e), which also implies that Eu anomalies represent authigenic signatures that were not significantly influenced by detrital material. Using a Ce/Ce*-Pr/Pr* cross-plot (Bau and Dulski, 1996), it is possible to identify true negative Ce anomalies (Supplementary Fig. 1b). On this basis, all IF and dolostone samples lack true negative Ce anomalies.

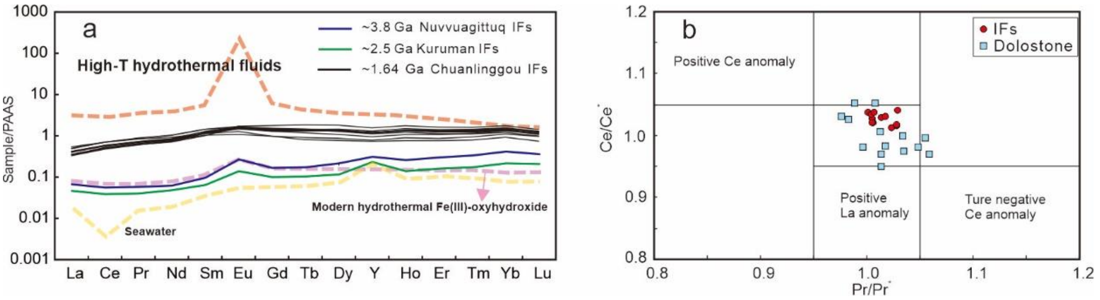

Supplementary Fig. 1. a. PAAS (Post-Archean Average Shale)-normalized REE+Y patterns for the Chuanlinggou IF. PAAS data from McLennan, 1989, average high-temperature hydrothermal fluids from Douville et al., 1999, average modern seawater from Bau et al., 1995, 1996, 3.8 Ga Nuvvuagittuq IFs from Mloszewska et al., 2012, 2.5 Ga Krunmman IFs from Bau et al., 1997. b. Ce/Ce* vs. Pr/Pr* diagram for the IF and dolostone samples (after Bau and Dulski, 1996). $Ce/Ce^* = 2\times Ce_{PASS}/(La_{PASS}+Pr_{PASS})$; $Pr/Pr^*=2\times Pr_{PAAS}/(Ce_{PAAS}+Nd_{PAAS})$.

In this study, the samples with the lowest organic contents were principally located in the IF and sandstone, where detrital organic matter, if any, might be present in a higher proportion, thereby potentially influencing $\delta^{13}C_{org}$ values (Johnston et al., 2012). For example, if detrital organic matter was ^{13}C-enriched relative to coeval marine organic matter, a higher ratio of detrital organic matter in the shallow water samples would induce much higher $\delta^{13}C_{org}$ values. However, we observe no relationship between Al content and TOC, and no positive relationship between Al content and $\delta^{13}C_{org}$ (Supplementary Figs. 2f and g), suggesting detrital organic matter is unlikely to influence $\delta^{13}C_{org}$ values. The $\delta^{13}C_{org}$ data from the studied samples fall within the typical range of early mid-Proterozoic strata in the central NCC (e.g., Guo et al., 2013; Luo et al., 2014). In addition, the absence of significant correlation between $\delta^{13}C_{org}$ and TOC (Supplementary Figs. 2h) in our samples suggests that the degradation of organic matter during metamorphic processes had limited effect on $\delta^{13}C_{org}$ values.

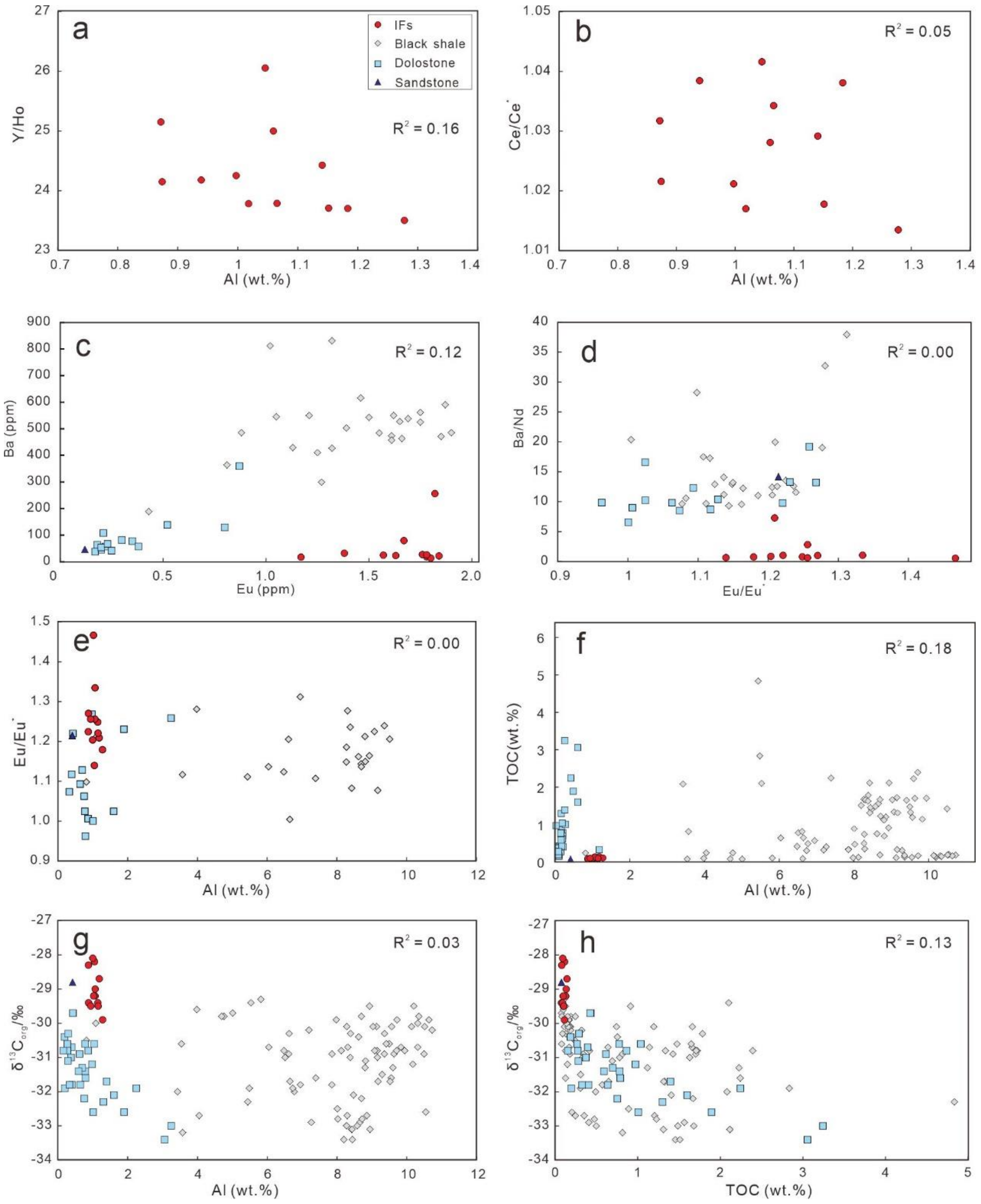

Supplementary Fig. 2. Binary variation diagrams for samples from the Chuanlinggou Formation. a. Al vs. Y/Ho. b. Al vs. Ce/Ce*. c. Ba vs. Eu. d. Eu/Eu* vs. Ba/Nd. e. Al vs. Eu/Eu*. f. Al vs. TOC. g. Al vs. $\delta^{13}C_{org}$. h. TOC vs. $\delta^{13}C_{org}$. One outlier is not shown in parts c and d.

References

Bau, M., Dulski, P., Möller, P., 1995. Yttrium and holmium in South Pacific seawater: vertical distribution and possible fractionation mechanisms. Chem. Dere-Geochem. 55, 1–15.

Bau, M., Dulski, P., 1996. Distribution of yttrium and rare earth elements in the Penge and Kuruman iron-formation, Transvaal Supergroup, South Africa. Precambrian Res. 79, 37–55.

Bau, M., Höhndorf, A., Dulski, P., Beukes, N.J., 1997. Sources of rare-earth elements and iron in Paleoproterozoic iron-formations from the Transvaal Supergroup, South Africa: evidence from neodymium isotopes. J. Geol. 105, 121–129.

Bau, M., Koschinsky A., Dulski, P., Hein, J.R., 1996. Comparison of the partitioning behaviours of yttrium, rare earth elements, and titanium between hydrogenetic marine ferromanganese crusts and seawater. Geochim. Cosmochim. Acta. 60(10), 1709–1725.

Chu, X.L., Zhang, T.G., Zhang, Q.R., Lyons, T.W., 2007. Sulfur and carbon isotope records from 1700 to 800 Ma carbonates of the Jixian section, northern China: implicationsfor secular isotope variations in Proterozoic seawater and relationships to global supercontinental events. Geochim. Cosmochim. Acta. 71, 4668–4692.

Dauphas, N., John, S.G., Rouxel, O., 2017. Iron isotope systematics. Rev. Mineral. Geochem. 82, 415–510.

Douville, E., Bienvenu, P., Charlou, J. L., Donval, J. P., Fouquet, Y., Appriou, P., Gamo, T., 1999. Yttrium and rare earth elements in fluids from various deep-sea hydrothermal systems. Geochim. Cosmochim. Acta. 63, 627–643.

Duan, C., Li, Y., Yang, Y., Liang, Y., Wei, M., Hou, H., 2018. U-Pb Ages and Hf Isotopes of Detrital Zircon Grains from the Mesoproterozoic Chuanlinggou Formation in North China Craton: Implications for the Geochronology of Sedimentary Iron Deposits and Crustal Evolution. Minerals 8, 547.

Dulski, P., 1994. Interferences of oxide, hydroxide and chloride analyte species in the determination of rare earth elements in geological samples by inductively coupled plasma-mass spectrometry. J. Anal. Chem. 350, 194–203.

Gao, L.Z., Zhang, C.H., Liu, P.J., Ding, X.Z., Wang, Z.Q., Zhang, Y.J., 2009. Recognition of Meso- and Neoproterozoic stratigraphic framework in North and South China. Acta Geosci. Sin. 30, 433–446 (in Chinese with English abstract).

Gao, L.Z., Zhang, C.H., Yin, C.Y., Shi, X.Y., Wang, Z.Q., Liu, Y.M., Liu, P.J., Tang, F., Song, B., 2008. SHRIMP zircon ages: basis for refining the chronostratigraphic classification of the Meso- and Neoproterozoic strata in North China Old Land. Acta Geosci. Sin. 29, 366–376 (in Chinese with English abstract).

Guo, H., Du, Y., Kah, L. C., Huang, J., Hu, C., Huang, H., Yu, W., 2013. Isotopic composition of organic and inorganic carbon from the Mesoproterozoic Jixian Group, North China: Implications for biological and oceanic evolution. Precambrian Res. 224, 169–183.

Johnston, D.T., Macdonald, F.A., Gill, B.C., Hoffman, P.F., Schrag, D.P., 2012. Uncovering the Neoproterozoic carbon cycle. Nature 483, 320–323.

Kendall, B., Reinhard, C.T., Lyons, T.W., Kaufman, A.J., Poulton, S.W., Anbar, A.D., 2010. Pervasive oxygenation along late Archaean ocean margins. Nat. Geosci. 3, 647–652.

Li, C., Planavsky, N.J., Love, G.D., Reinhard, C.T., Hardisty, D., Feng, L., Bates, S.M., Huang, J., Zhang, Q., Chu, X., 2015. Marine redox conditions in the middle Proterozoic ocean and isotopic constraints on authigenic carbonate formation: Insights from the Chuanlinggou Formation, Yanshan Basin, North China. Geochim. Cosmochim. Acta. 150, 90–105.

Li, H.K., Lu, S.N., Su, W.B., Xiang, Z.Q., Zhou, H.Y., Zhang, Y.Q., 2013. Recent advances in the study of the Mesoproterozoic geochronology in the North China Craton. J. Asian Earth Sci. 72, 216–227.

Li, Z.H., Zhu, X.K., 2012. Geochemical features of Xuanlong type iron ore deposit in Hebei Province and their geological significances. Acta Petrol. Sinica 28(9), 2903–2911.

Lin, Y., Tang, D., Shi, X., Zhou, X., Huang, K., 2019. Shallow-marine ironstones formed by microaerophilic iron-oxidizing bacteria in terminal Paleoproterozoic. Gondwana Res. 76, 1–18.

Lu, S.N., Li, H.M., 1991. A precise U-Pb single zircon age determination for the volcanics of Dahongyu Formation, Changcheng system in Jixian. Acta Geosci. Sin. 22, 137–145 (in Chinese with English abstract).

Luo, G.M., Junium, C.K., Kump, L.R., Huang, J.H., Li, C., Feng, Q.L., Shi, X.Y., Bai, X., Xie, S.C., 2014. Shallow stratification prevailed for 1700 to 1300 Ma ocean: evidence from organic carbon isotopes in the North China Craton. Earth Planet. Sci. Lett. 400, 219–232.

McLennan, S.B., 1989, Rare earth elements in sedimentary rocks: Influence of provenance and sedimentary processes. In: Lipin B. R., McKay G. A. (Eds.), Geochemistry and Mineralogy of the Rare Earth Elements. Mineral. Soc. Am., Spec. Pap., 169–200.

Mloszewska, A.M., Pecoits, E., Cates, N.L., Mojzsis, S.J., O'Neil, J., Robbins, L.J., and

Konhauser, K.O., 2012, The composition of Earth's oldest iron formations: The Nuvvuagittuq Supracrustal Belt (Québec, Canada). Earth Planet. Sci. Lett. 317–318, 331–342.

Planavsky, N.J., McGoldrick, P., Scott, C.T., Li, C., Reinhard, C.T., Kelly, A.E., Chu, X.L., Bekker, A., Love, G.D., Lyons, T.W., 2011. Widespread iron-rich conditions in the mid-Proterozoic ocean. Nature 477, 448–495.

Sun, H.Y., Gao, L.Z., Bao, C., Chen, Y.L., Liu, D.Y., 2013. SHRIMP zircon U-Pb of Mesoproterozoic Chuanlinggou Formation from Kuancheng County in Hebei Province and its geological implications. Acta Geol. Sin. 87, 591–596 (in Chinese with English abstract).

Tang, D.J., Shi, X.Y., Liu, D.B., Lin, Y.T., Zhang, C.H., Song, G.Y., Wu, J.J., 2015. Terminal Paleoproterozoic ooidal ironstone from North China: a sedimentary response to the initial breakup of Columbia Supercontinent. Earth Sci. - J. China Univ. Geosci. 40, 290–304 (in Chinese with English abstract).

Zhang, K., Zhu, X., Wood, R.A., Shi, Y., Gao, Z., Poulton, S.W., 2018. Oxygenation of the Mesoproterozoic ocean and the evolution of complex eukaryotes. Nat. Geosci. 11, 345–350.

Zhang, S.H., Zhao, Y., Ye, H., Hu, J.M., Wu, F., 2013. New constraints on ages of the Chuanlinggou and Tuanshanzi formations of the Changcheng System in the Yan-Liao area in the northern North China Craton. Acta Petrol. Sin. 29, 2481–2490 (in Chinese with English abstract).

Zhang, Y.B., Li, Q.L., Lan, Z.W., Wu, F.Y., Li, X.H., Yang, J.H., Zhai, M.G., 2015. Diagenetic xenotime dating to constrain the initial depositional time of the Yan-Liao Rift. Precambrian Res. 271, 20–32.